Three-dimensional mapping of the benthic invertebrates biophony with a compact four-hydrophones array

C. Gervaise [a,*], J. Lossent [a,c], C.A. Valentini-Poirier [d], P. Boissery [d], C. Noel [e], L. Di Iorio [a,b]

[a] CHORUS Research Institute, Phelma Minatec, 3 Parvis L. Neel, 38000 Grenoble, France
[b] Foundation of the Grenoble Institute of Technology, 46 Rue Felix Viallet, 38000 Grenoble, France
[c] Univ. Grenoble Alpes, CNRS, Grenoble INP, GIPSA-lab, 38000 Grenoble, France
[d] French Water Agency Rhône Méditerranée Corse (RMC), Imm Le Noailles 62 La Cannebière, 13001 Marseille, France
[e] SEMANTIC T.S., Acoustics, Oceanography, Environment Engineering Consulting Center, 1142 Chemin Saint-Roch, Sanary-sur-Mer, France

ABSTRACT

Benthic invertebrates emit broadband transient sounds, that dominate coastal soundscapes and can inform on the environment and its ecological state. Numerous works have studied temporal patterns of Benthic Invertebrate Biophonies (BIB) and linked them to environmental parameters or ecological processes, but there is a lack of knowledge about the spatial variability of BIB. Here, we mapped Benthic Invertebrate Sounds (BIS) in three dimensions using a compact array (2 m × 2 m × 2 m) of four hydrophones within the scope of eco-acoustics studies. Firstly, we developed tools to localize any individual sound emitted by benthic invertebrates. A theoretical calculation of the Cramer Rao Bounds (CRB) consolidated by *in situ* active emissions from known positions, demonstrated the accuracy of the localization. Secondly, by accumulating all the positions of the BIS recorded during a night, three methods are proposed to map the BIB at different spatial scales. An *in situ* measurement campaign carried out on a 300 m × 300 m artificial reef system revealed that the marine fauna was binary spatially distributed: rich and numerous on artificial reefs and poor and weak outside the reefs. At small ranges (10 m), the acoustic maps matched the geometric structures of the reefs with an accuracy of 0.5 m. At large scales (100 m and 300 m), the acoustic hot-spots on the maps corresponded to distant reefs, with an accuracy of 7 m and 10 m respectively.

This study provides the first maps of the BIB at ecologically relevant scales and shows that they can be used to identify, quantify, follow and track benthic activity hot-spots. In combination with biological and ecological information, passive acoustic monitoring using such maps can be a powerful complementary tool for ecological studies, such as the quantification of grazing activity or the evaluation of the efficiency of marine ecologic restoration programs.

© 2018 Elsevier Ltd. All rights reserved.

1. Introduction

The underwater soundscape is a collection of sounds that emanate from a marine seascape or propagate through it [1]. It is composed of natural ambient sounds (geophony, [2–4]), anthropogenic sounds (anthrophony, [5,6]) and sounds from marine fauna (biophony). The main contributors to the biophony are cetaceans [7], fishes [8–10] and benthic invertebrates. Benthic invertebrates emit a biophony consisting of many isolated broadband transient sounds. Snapping shrimps (*Alpheidae* spp.) produce among the loudest sounds in marine coastal environments [11] dominating

their soundscapes [12,13]. However, other invertebrates such as sea urchins [14], crustaceans [15], bivalves [16] and generally speaking benthic populations [17] are also known to produce audible and distinct acoustic signals that contribute to the Benthic Invertebrate Biophony (BIB).

The technological developments achieved over the last decade have made it possible to create a commercial offer of reliable, cost-effective and autonomous acoustic recorders that can record soundscapes over periods long enough to cover different biological rhythms [18]. By taking advantage of the good capabilities of autonomous acoustic recorders and the high informational content and integrative nature of soundscapes, eco-acoustics or soundscape ecology infers ecologically relevant information on ecosystems [19,20]. Over the last five years, numerous works have

---

* Corresponding author.
E-mail address: cedric.gervaise@chorusacoustics.com (C. Gervaise).

demonstrated the interest of eco-acoustics for the study of coastal marine ecosystems (e.g., [21]).

One of the key emerging areas identified by the scientific community is the fine characterization of the spatial variability of soundscapes allowing to produce sound-maps of acoustic habitats [22]. Such acoustic maps must be adapted to ecological scales. The spatial variability of benthic communities of coastal habitats has been shown to be significant at small scales (i.e., between one meter and one kilometer) for a wide diversity of habitats, including hard bottom substrates [23–25], rocky and coral reefs [26], or seagrass [27]. These spatial scales coincide with the ones of negative disturbances through human activities, but also of positive ecological restoration actions such as artificial reefs [28]. Assessing settlement mechanisms of artificial reefs for instance, constitutes a general problem for the evaluation of their efficiency [29,30]. On a large scale, it is necessary to know whether artificial reefs concentrate local fauna or whether they create biomass [31], and how these reefs attract species [32]. At smaller scales, inside the reefs, it is necessary to understand how species and biomass production are distributed according to the type of reef [33–38].

Estimating the spatial variability of a soundscape for ecological studies requires the biophonic sources to be localized and mapped in terms of 'acoustics richness' (number of different sounds), 'acoustics abundance' (number of sounds of the same type) and 'acoustics loudness' (sound level of the sounds). It is a challenging task because biological sound production is perceived after propagating between the source and the recording system [39]. In fact, as the sounds of different sources constituting the BIB cover a very wide dynamic of propagation ranges (from one meter to more than one kilometer, [11,14,17]), an acoustic recorder with a single isotropic hydrophone reports simultaneously on weak sources close to the measurement point and distant but loud sources. This is a major drawback when it comes to identifying spatial variability at scales below the propagation range of biological sound sources [40–42]. This problem can be solved if the recording systems have the capability to locate the sound they record and detect. All methods of passive acoustic localization are based on the same principle: the use of several hydrophones to detect and date the arrival of a signal, followed by the computation of the Time Of Arrival Differences (TOAD) of the signal between each couple of hydrophones, and finally the assessment of the position (geographical coordinates, directions of arrival) of the source compatible with the TOAD. Depending on the number of hydrophones used and their geometry, the localization process can provide absolute coordinates or directions of arrival [43,44]. There are a small number of studies on localization and mapping of BIB for environmental purposes reported in the literature. Pioneering works in the early nineties showed the possibility of mapping benthic sound production by passive acoustics and of using the masking created by an object placed in this sound field to detect its presence and to represent its shape [45–47]. For these studies, a parabolic antenna of 3 m diameter with 130 hydrophones was used. This type of system is not compatible with the budgetary and operational constraints of environmental studies, but has demonstrated the interest of multi-sensor technology for the three-dimensional mapping of BIB. To our knowledge, three studies [11,43,48] used low-cost and more operational instrumentation to describe the directionality of the biological noise of coastal ecosystems in the horizontal plane as a function of the azimuth. These studies did not describe a three-dimensional mapping of the BIB. The directionality of BIB in the vertical axis was only addressed by D'Spain and Batchelor [49], who established a map of BIB in azimuth and elevation. However, the system used was complex, composed of a planar antenna of 6 m height and 0.6 m width, on which 131 sensors were distributed. Furthermore, the algorithm used for data processing was specific to the system.

In this paper, we address the issue of the three-dimensional localization and mapping of the BIB of coastal ecosystems with an operational device for spatial scales ranging from 1 m to 300 m. The originality of this work remains both in the developed processing tools and in their applications to real data. More specifically, our objectives are:

- To propose a method for detecting and locating an individual benthic sound source in elevation and azimuth from a simple, operational, compact network of four hydrophones, and to assess its accuracy.
- To propose three methods for mapping BIB measured over a significant period of time (i.e. one night) for scales ranging from 1 m to 300 m.
- To apply these methods on real data from artificial reefs with the aim to illustrate the output of our tools, to assess their performances and to evaluate the future potential of passive acoustic 3D monitoring for ecological applications such as ecological restoration programs.

Part one presents the real data collected using multiple compact monitoring systems composed of four sensors deployed close to artificial reefs. Part two presents the method of localization in elevation and azimuth of individual Benthic Invertebrate Sounds (BISs) and evaluates its accuracy via the theoretical framework of Cramer Rao Bounds (CRB) and the use of real data involving active emissions from known positions. Part three proposes three methods to map BIB based on azimuth and elevation from sources located on a vertical known surface and on the seafloor. Part four illustrates the three mapping methods using real data from an artificial reef system and part five is devoted to discussions of two topics: the performance of the presented tools and their contribution in terms of eco-acoustic analyses.

2. The Prado2015 sampling campaign

The acoustic sampling campaign called "Prado2015" was carried out in September 2015 as part of the SEACOUSTIC research project conducted in collaboration with the French Water Agency Rhône Méditerranée Corse. The field site was the largest Mediterranean artificial reef system situated in the Bay of Marseille, France (5° 335′ E, 43.267 N, Fig. 1). The Prado reef system was set up in 2008 to recreate a productive ecosystem and a complete trophic chain over a wide area of dead matte comprised within a depth range of 20 and 30 m. In this area, the *Posidonia oceanica* seagrass disappeared due to cumulative anthropic pressures from 1960 to 2008. The reef system expands over 2.2 km^2 and consists of 401 modules of 6 types organized in 6 villages [50]. The Prado reef system represents an appropriate field test site for the here-proposed work as it presents very contrasting acoustic scenes between the reef system's modules, with highly soniferous benthic fauna, and the poor surrounding dead matte [12,51,52]. Furthermore, there is good environmental knowledge of the site, as the positions, the type of artificial reefs are known, and a precise side-scan sonar survey has been realized.

For this study, we focused on village 6 (Fig. 1) and two types of modules, the ROCKS and the FAKIR reef (Fig. 2). A recording array (1.8 m × 1 m × 1.8 m) called "Cyclope" consisting of four hydrophones distributed in 3D was systematically positioned at a distance of 3 m South of each studied module (Fig. 3). Table 1 provides the coordinates of the hydrophones in the local coordinate system identified in Fig. 3. The four hydrophones of the "Cyclope" (HTI 92 WB of High Tech Inc.® with a sensitivity equal to −155 ±3 dB re 1 µPa/1 V on the frequency band [5 Hz, 50 kHz]) were connected to an autonomous SDA 14 recorder of the company RTSYS®. The recorder ensured the continuous
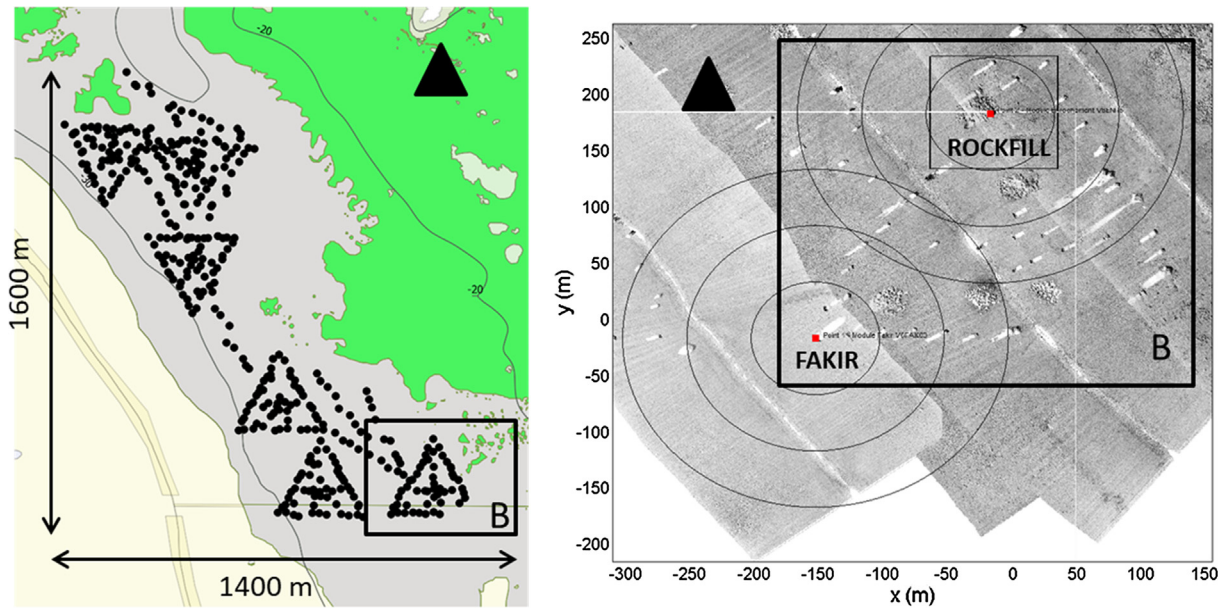
Fig. 1. Left: Map of the Prado reef system consituted of 401 artificial reefs (black points), Marseille, France (5°33504 E, 43°26810 N) organized in 6 villages and 3 connections between the villages. In green: *Posidonia oceanica* meadows, in grey: dead matte, in beige: sandy bottom, black thin lines: 20 m and 30 m isobaths. Right: zoom on village n°6 (box B) with a grey scale side-scan sonar map. Black pixels followed by white pixels identify reefs (black pixels) and their shadows (white pixels), red squares: recording positions, three meters southward from a FAKIR and a ROCKS reef. The circles around FAKIR and ROCKS reefs correspond to a 50 m, a 100 m and a 150 m radius. (For interpretation of the references to color in this figure legend, the reader is referred to the web version of this article.)
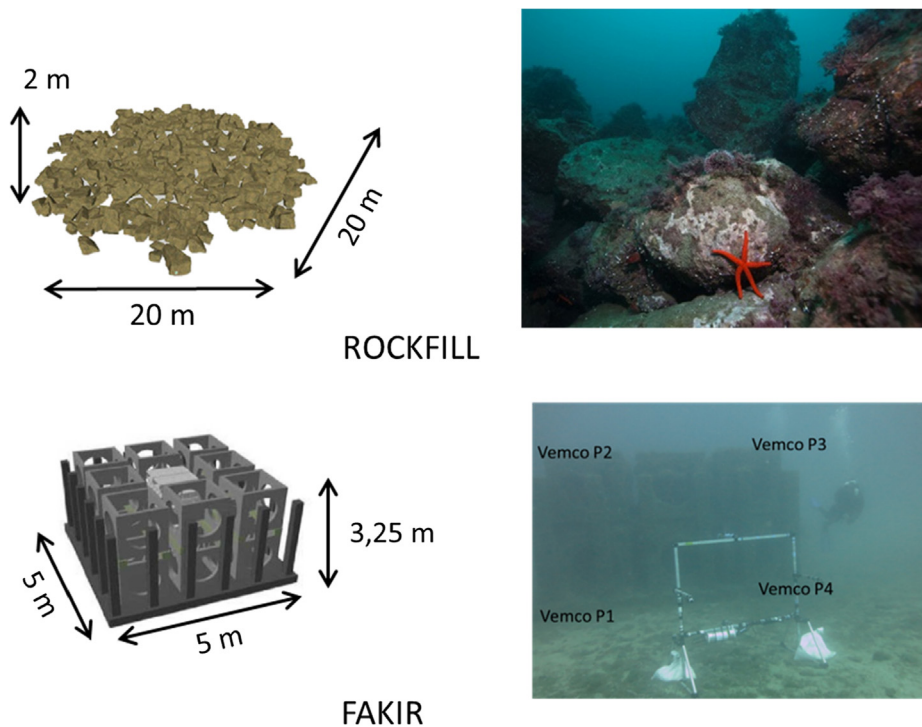

Fig. 2. Description of the two artificial reefs monitored in this study. Top: artificial reef of type ROCKS, a 20 m × 20 m × 2 m pile of rocks. Bottom: artificial reef of type FAKIR, a 5 m × 5 m × 3.25 m complex concrete structure. The photo at the bottom right also shows the compact recording structure 'Cyclope' with four hydrophones as well as the positions of the active emissions (VEMCO P1 to VEMCO P4) (graphic representations from [64], photo credit of the ROCKS reef: S. Ruitton (MIO), photo credit of the FAKIR reef: CHORUS).

acquisition on four synchronized channels for 10 h from 9 p.m. to 7 a.m. at a sampling frequency of 156250 Hz, 24-bit resolution for ±2.5 V dynamics, and with the recorder set at 0 dB gain. Measurements for the ROCKS reef were carried out from 24/09/2015 to 25/09/2015, whereas measurements for the FAKIR reef were conducted from 29/09/2015 to 30/09/2015.

During the entire campaign, winds were relatively high (26.8 ± 4 km/h, Manuel Anemometer Xplorer XP01-Skywatch©) from the Northwest, but the bay of Marseille is well sheltered and thus poorly affected. The mean surface temperature was 21 ± 0.5 °C and the mean temperature on the seabed was 15.8 ± 0.7 °C (CTD probe RBR concerto 103 serial number 60336).
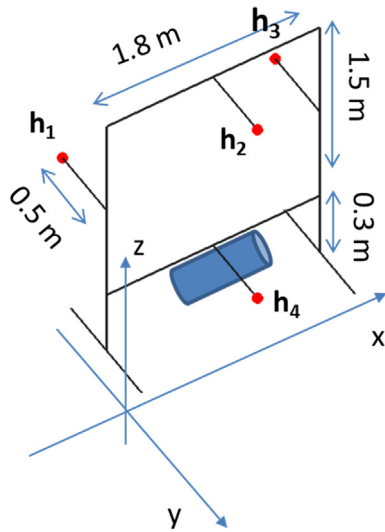
Fig. 3. Geometry of the "Cyclope" compact array of four hydrophones (red points h_1 to h_4) connected to a RTSYS SDA 14 autonomous recorder (blue cylinder). (For interpretation of the references to color in this figure legend, the reader is referred to the web version of this article.)

Table 1
Coordinates of the four hydrophones of the "Cyclope" recording array in its local coordinate system (x_l, y_l, z_l).

Hydrophone	x (m)	y (m)	z (m)
C_1	0.00	0.50	1.05
C_2	0.90	−0.50	1.80
C_3	1.80	0.50	1.05
C_4	0.90	−0.50	0.30

The positions and types of modules, the bathymetry of the zone and the habitat maps were provided by the town of Marseille (with the courtesy of E. Medioni, City of Marseille). After the set-up of the artificial reef system, a map of the artificial reef villages was carried out by SEMANTIC TS using a towed active side-scan sonar Klein 450 kHz. A side-scan sonar maps the reflectivity of the seafloor and objects on the seafloor in the perpendicular direction to the trajectory of the towing boat (for more details about side-scan sonar see Blondel [53]). The side-scan sonar is operated near the bottom (10 m elevation), and maps are well adapted to detect and locate the artificial reefs with a resolution of 20 cm and an accuracy of 2 m. The side-scan sonar map was provided for this study by the City of Marseille (with the courtesy of E. Medioni) and is considered as the best ground truth data to calibrate the here-presented passive acoustics maps of the BIB.

3. First processing stage: Detection and localization of a single BIS

The first processing stage tackles the detection and the localization of benthic sounds by means of a compact array of four hydrophones. It relies on the specific nature of the BIB: a succession of short transient sounds with a large frequency bandwidth ranging between 1.5 kHz and more than 70 kHz [14,17,54] (Fig. 6, e.g., plot P_1).

3.1. Conventions and mathematical notations

The origin of a Cartesian coordinate system {x, y, z} was placed at the center of the array (Fig. 4). The x and y axes are horizontal, with the x oriented to the East and the y oriented to the North. The z axis is vertical, facing the surface. To this Cartesian coordinate system we associated a spherical coordinates system {R, α, θ}. A source positioned at $\{x_s, y_s, z_s\}$ produces a sound with a direction of arrival with respect to the recording array described by 2 angles: the azimuth α_s that measures the angle between the East and the projection of the direction of arrival on the horizontal plane (positive towards the North), and the elevation θ_s that measures the angle between this projection and the direction of arrival in the vertical plane (positive upwards). In order to cover the entire space, the azimuth ranges between −180° and +180° and the elevation between −90° and +90°. This solid angle of 4π steradians gathers all possible directions of arrival. It is discretized in elementary pixels P centered on a specific direction $\{\alpha_0, \theta_0\}$ with an angular aperture $d\alpha$ for the azimuth and $d\theta$ for the elevation. These elementary pixels are plotted on a sphere of unitary radius around the recording array.

3.2. Algorithm to localize an individual BIS

We worked at the temporal scale of an individual BIS. The objective was to detect, date, locate single BISs and calculate their acoustic features. Fig. 5 shows the implemented processing.

We suppose that the BIS $e(t)$ emitted by the source arrives at each sensor of the recording array attenuated and hidden in noise as well as delayed by the time of propagation of the sound between the position of the source and the receiver. The signal measured by one of the four hydrophones is:

$$s_i(t) = \frac{1}{R_{si}} e(t - \tau_{si}) + b_i(t) \tag{1}$$

with $\tau_{si} = \frac{R_{si}}{c}$, $\tag{2}$

$$R_{si} = \sqrt{(x_s - x_{ci})^2 + (y_s - y_{ci})^2 + (z_s - z_{ci})^2} \tag{3}$$

and $bi(t)$ being the noise at the sensor "i", c being the sound velocity in the water, R_{si} being the distance between the source and the sensor i with the coordinates $\{x_{ci}, y_{ci}, z_{ci}\}$, and τ_{si} being the time it takes for the emitted sound to reach the sensor i.

The detection of the BIS $e(t)$ and the measurement of its Time Of Arrival (TOA) were carried out for each of the four acquisition channels within an identical functional block B1 (Fig. 5). Within this block B1, the signal was first filtered on the frequency band of the BIB [1.5, 70 kHz] (C1, Fig. 5) and the local energy of the signal was then calculated by summing the squared filtered signal (C2, C3, Fig. 5). From this time series of acoustic energy, the Ambient Noise Level (ANL) was estimated (C4, Fig. 5) using the method described in Kinda et al. [55]. A Constant False Alarm Rate (CFAR) stage [56] (C5, Fig. 5) used this ANL and a target false alarm probability to calculate a detection threshold based on the energy of the signal (C6, Fig. 5). Details of the calculations in C4 and C5 are presented in Appendix A. If the local energy was higher than the detection threshold, then a BIS was detected. Its TOA was estimated as the start time of the BIS, i.e. the first instant at which the energy exceeds the threshold (C7, Fig. 5). The choice of this first instant allows robustness against reverberation that is usually high in shallow water environments. This treatment was replicated on the four measurement channels and for each sample.

If D is the greatest possible distance between sensors in the recording array, then the TOADs of the same BIS between sensors are between −D/c and +D/c. We discretized the acoustic recordings in segments of 2D/c width, with centers regularly spaced by a step δt (δt < 0.5D/c). A time segment was only selected if it contained one single BIS detected on each sensor (B2, Fig. 5).

To avoid taking into account the reverberation, BIS detections on the four acquisition channels can be rejected. (B3, Fig. 5). The
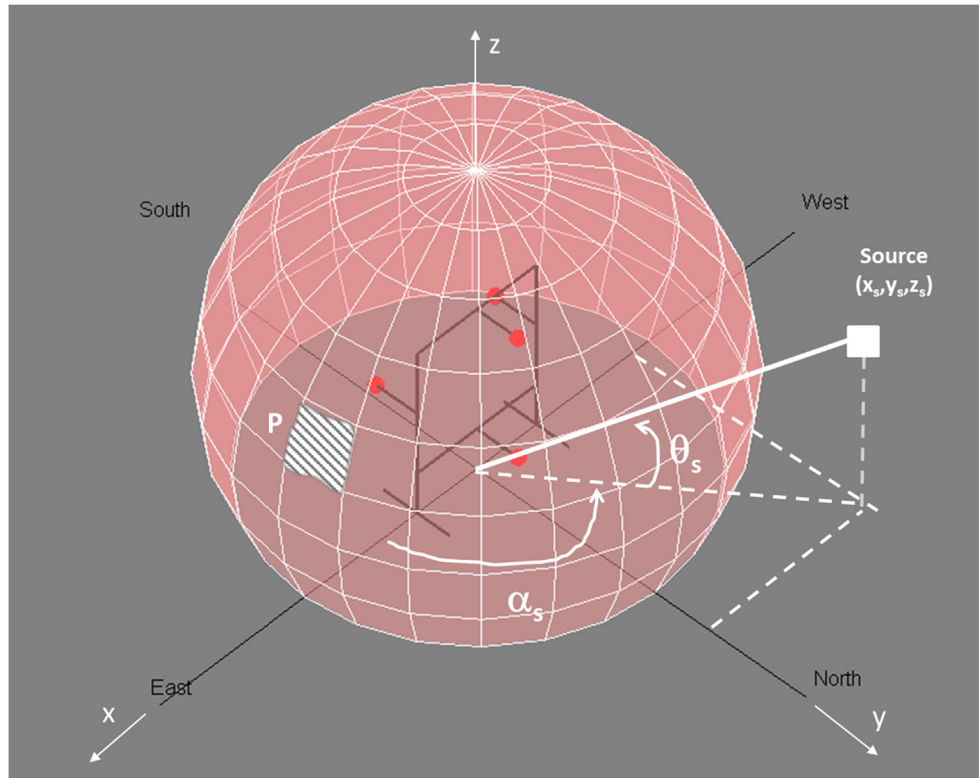
Fig. 4. Geometrical and angular conventions and mathematical notations. {xs, ys, zs} are the Cartesian coordinates of the sound source location. α_s represent the azimuth and θ_s the elevation of the sound source's location. P is the elementary pixel P centered on a particular direction {α_0, θ_0} with an angular aperture {dα, dθ}.
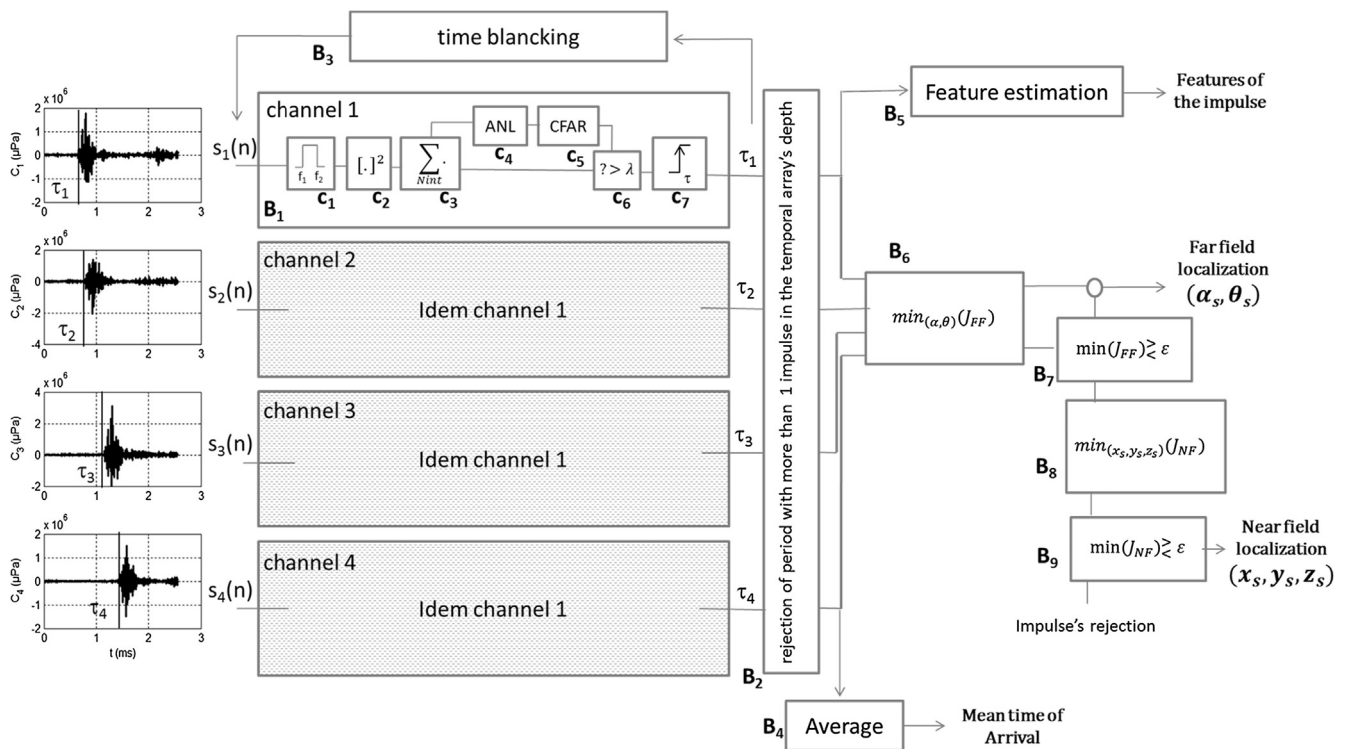
Fig. 5. Architecture of the proccessing chain of an individual BIS: detection, dating, localization and estimation of its acoustic features. The input signals of the chain are the measurements of the 4-hydrophones of the real BIS shown in Fig. 6.

arrival date of the BIS on the array was calculated as the average of the TOAs on the four sensors (B4, Fig. 5). This arrival time constitutes the first output of the processing chain and was also used

for post-processing to count the number of BISs in a unit of time. A pre-defined set of features of the BISs was calculated for each acquisition channel and averaged (B5, Fig. 5). This set of features

constitutes the second output of the processing chain. In this study, we calculated the broadband Sound Pressure Levels SPL_{RMS} and $SPL_{peak-to-peak}$ (dB re 1 µPa) of each detected BIS.

The localization algorithm is based on the TOAs of the BIS on the four sensors. The algorithm proposed here consists of two steps. In step one, the BIS is supposed to be far enough to produce a plane wave ensonifying the recording array. In this case, we only look for the azimuth and the elevation of the source (i.e., the bearing), which define the "position of the source" (B6 & B7, Fig. 5). We form six independent TOADs (TOAD τ_{21}, τ_{31}, τ_{41}, τ_{32}, τ_{42}, τ_{43}) from the four measured arrival times of the BISs that are defined by:

$$\{\tau_{ji} = \tau_j - \tau_i, (i,j) \in [1,4] \times [1,4] \wedge j > i\}.$$

From the theoretical expression of the TOAD of the BIS as a function of the supposed azimuth and elevation of the source (Appendix B), we form an agreement criterion J_{FF} ("Far-field") between the measured TOAD and the theoretical TOAD:

$$J_{FF}(\alpha, \theta) = c \times \sqrt{\sum_{\substack{i,j=1 \\ j>i}}^{4} (\tau_{ji} - \tau_{ij}(\alpha, \theta))^2} \qquad (4)$$

The position of the source (α_s, θ_s) is the one that minimizes J_{FF}. The minimization is carried out by an exhaustive search on an azimuth grid ranging from $-180°$ to $180°$, in steps of $0.1°$, and an elevation grid ranging from $-90°$ to $90°$, in steps of $0.1°$. If the minimum value of J_{FF} is small, then we assume (i) that the plane wave hypothesis is valid and (ii) that the position of the source is the pair (α, θ) minimizing J_{FF}. In the opposite case, if the minimum of J_{FF} remains high, the plane wave and the far-field source hypothesis are rejected. Consequently, the hypothesis of a close source, generating a spherical wave, is taken into account (B8 & B9, Fig. 5). The retained threshold ε for the residual acceptable difference after minimization is five centimeters and it corresponds to both: (i) a TOAD measurement error of five samples, i.e. 64 µs and (ii) a conservative estimation of the localization error of the sensors.

At the beginning of the process and once for all, we computed the map of the TDOA versus the elevation and the azimuth over this grid. During the process, for each transient sound, this pre-computed map was used to look for the elevation and azimuth that minimize the difference between the measured TDOA and the pre-computed map of modeled TDOAs. This represents an efficient and fast solution that does not suffer from the presence of local minima. 12 h of data were processed in six hours using MATLAB routines on a common laptop. The use of an optimization method in the case of the here-proposed method is only necessary real time processing was required and the processor's memory was insufficient to host the pre-processed map. In such a case, to search for the minimum, a pre-computed $5°$ low-resolution grid would be recommended followed by an optimization method initialized by this "low-resolution" minimum.

For the near-field localization under the hypothesis of a spherical wave, the position of the source is defined by its Cartesian coordinates $\{x_s, y_s, z_s\}$ and follows a theoretical model of the TOAD as a function of the position of the source (cf. Eqs. (1)–(3)). The position is obtained by minimizing the criterion J_{NF} ("Near Field") as follows:

$$J_{NF}(x, y, z) = c \times \sqrt{\sum_{\substack{i,j=1 \\ j>i}}^{4} (\tau_{ji} - \tau_{ij}(x, y, z))^2} \qquad (5)$$

The minimization is carried out by exhaustive exploration on a cubic grid in x, y, z, ranging from $-5D$ to $+5D$ in each direction in steps of 0.2 m, with D being the maximum distance between the sensors of the array, which corresponds to ±10 m for the "Cyclope" used in the Prado2015 campaign. If the value of J_{NF} at its minimum is greater than the threshold ε, then we assume that the source was not correctly located, both under the far-field hypothesis and the near-field hypothesis. In this case, the BIS is rejected. This case can occur if the TOAD are poorly estimated or if the sensors did not detect the same BIS in the selected segment. Blocks B6, B7 or B8, B9 provide the third output of the processing chain. We computed the map of the TDOA versus x, y, z of the source at the beginning of the process and this pre-computed map was used for each transient sound.

Numerical simulations (not shown here) demonstrate that the sources inside the volume of the recording array and in its near vicinity (distance from the center less than 2D) are located in the near-field, whereas the BIS emitted at a distance greater than 2D are in the far-field.

3.3. Accuracy of the estimation of the azimuth and the elevation – The far-field case

To study the accuracy of our localization method we combined a theoretical approach with an experimental demonstration. For the experimental demonstration, we used a VEMCO® V16 synthetic pulse transmitter producing a pulses train every 20 s. Each pulse has a peak frequency of 63 kHz, duration of 5 ms and a Source Level (SL) of 150 dB re 1 µPa rms at 1 m. These features are close to the ones of natural BIS. The VEMCO pulse transmitter was placed on three of the corners of the FAKIR reef (Fig. 2). 300 pulses were emitted during two minutes at each corner.

For the theoretical approach, the angular accuracy was estimated according to the Cramér-Rao Bounds (CRB) theory [57]. Under the hypothesis of a white and Gaussian noise added to the theoretical TOAD, the CRB are lower bounds of the variance of any unbiased estimator of the azimuth and elevation of the source to be localized. Asymptotically, when the Signal-to-Noise-Ratio (SNR) tends to infinity, the variances of the azimuth and elevation estimators resulting from minimizing the criterion J_{FF} (Fig. 5, block B7) tend towards the CRB. The derivation of the CRB is detailed in Appendix B. One of the inputs needed for the calculation of the CRB is the standard deviation of the TOAD estimated from the real data. For this, we included a significant number of BIS. For each one, thanks to the measurements taken just before the time of arrival (Fig. 6, plot P_0, step 1) we estimated the variability of the ambient noise level (σ, Fig. 6, plot P_0) and plotted it on the rising edge of the envelope of the BIS (Fig. 6, plot P_0, step 2). Then we computed the temporal exploration of this footprint as a good indication of the measurement error of the TOAD (σ_τ, Fig. 6, Plot P_0). Fig. 6 illustrates this process on two real transient sounds, one from the VEMCO tag (arrow a_1, plot P_1) and the other one from a benthic invertebrate (arrow a_2, plot P_1). The plots P_2 and P_3 present a 8 ms segment containing the transient sounds. On plot P_2, the VEMCO sound starts at 0.75 ms and lasts 5 ms while the BIS starts at 2 ms and last 0.25 ms (plot P_3). Although the sounds have not the same duration, a zoom on a 1-millisecond segment at the beginning of the signals (i_1, i_2 on plots P_2, P_3, Fig. 6) indicates that they have the same rising edges (plot P_4 and P5 where time is relative to the center of the segment i_1 or i_2). Using this method, we found that the standard deviation of the TOAD measurements was 10 ± 2 samples (N = 88), i.e. 64 µs ± 12 µs both for natural BIS and synthetics VEMCO emissions.

The calculation of the CRB was carried out for the geometry of the "Cyclope" for azimuths varying between 0 and 360° and elevations varying between $-90°$ and $+90°$. Fig. 7 presents the results. The standard deviation on the azimuth has the vertical as an axis of symmetry; it is minimal for a rise of $0°$ and increases as the elevation increases (Fig. 7a). For elevations between $-10°$ and $50°$, the standard deviation of the azimuth is about $2.5°$. The standard deviation on the elevation varies little, and is of the order of $2°$ (Fig. 7b). Elevation and azimuth can be estimated simultaneously, as the
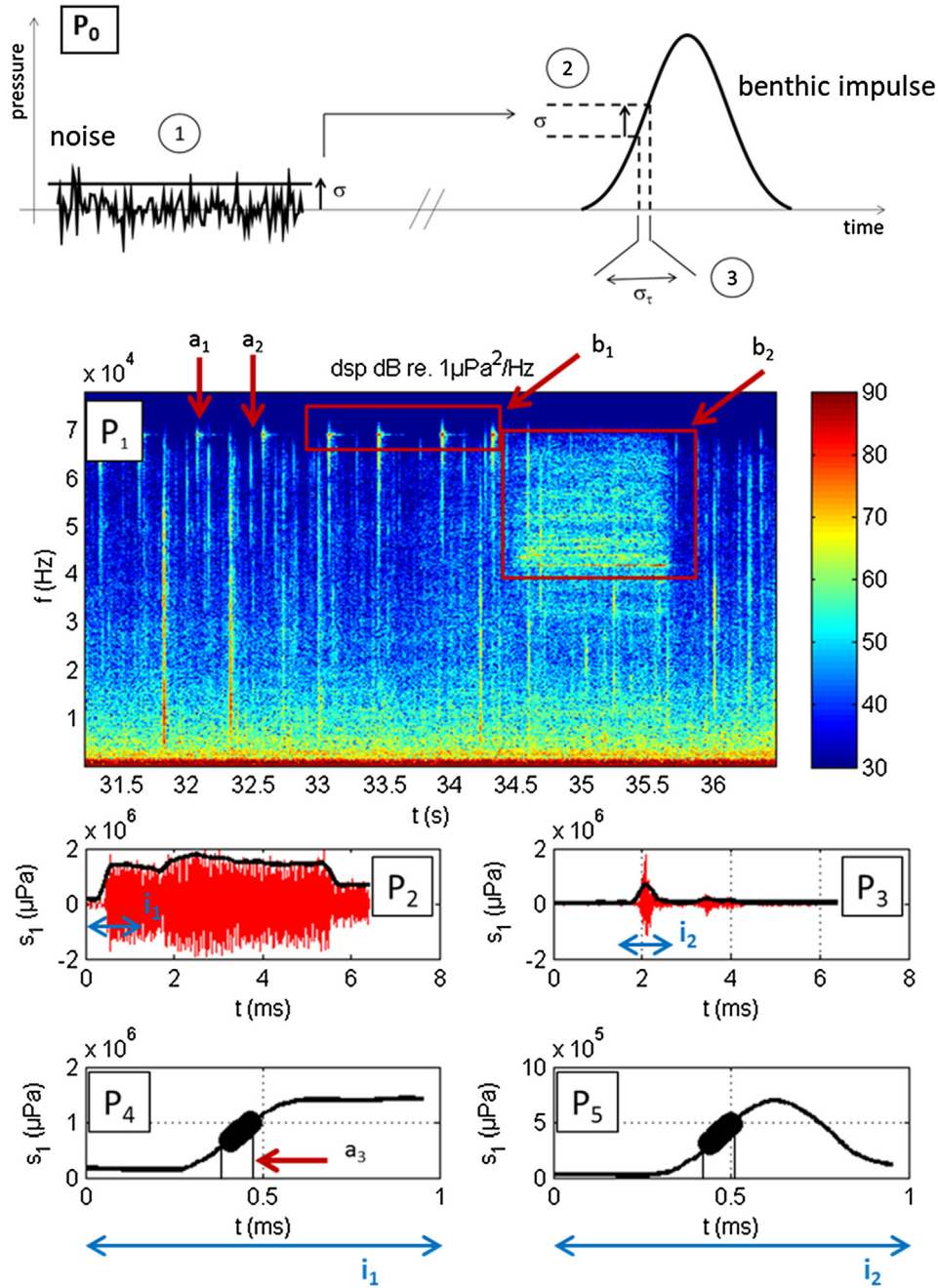
Fig. 6. Process to estimate the standard deviation of the time of arrival of a typical BIS from the FAKIR module during calibration with the VEMCO. P0: process to estimate the standard deviation of the time of arrival (3) with an estimate of the variability of the noise (1) superimposed to the rising edge (2) of a transient sound, P1: Spectrogram (LFFT = 8192, REC = 0.9, Kaiser 180 dB), box b1: synthetic emission of the VEMCO tag, box b2: Noise of the diver's regulator, arrow a1: emission of the VEMCO tag studied in the plots P2 and P4, arrow a2: BIS studied in the plots P3 and P5. Plots P2, P3: waveforms in red and envelope in black of the VEMCO emission and the BIS, plots P4 and P5: 1 ms zoom (relative time) of the rising edge of the BIS envelope (black line) and the imprint of the variability of the ambient noise (black oval) allowing to determine the error of measurement of the arrival time (arrow a3). (For interpretation of the references to color in this figure legend, the reader is referred to the web version of this article.)

correlation coefficient between the two parameters is close to 0 (±0.05) (Fig. 7c).

Fig. 6 shows that the rising edges of the VEMCO tag emissions as well as the BISs and the variances of their TOAD are equivalent. Consequently, the synthetic signals of the VEMCO tag can be used to study experimentally the azimuth and elevation localization errors and estimate the accuracy of the here-proposed method. The azimuth and elevation localization algorithm was applied to VEMCO emissions with a SNR greater than 13 dB. Fig. 8 illustrates the results. The successive VEMCO emissions were on average centered on the target's theoretical position, therefore fully validating

the numerical implementation of the here-proposed mapping method. 300 pulses were located per corner of the module. The standard deviations for the three corners were 2.9°, 3.4° and 3.6° for the azimuth and 3.8°, 4.2° and 3.51° for the elevation respectively. These values measured *in situ* are of the same order of magnitude as the CRBs (+∼1°). Consequently, the similitudes between the CRB theoretical approach and the VEMCO field approach fully validate the accuracy assessment. The accuracy of the localization process in azimuth and elevation is of the order of 3°, representing a spatial accuracy of 0.15 m for an emission located at 3 m of the recording array, 0.5 m at 10 m, 2.6 m at 50 m, 5.2 m at 100 m
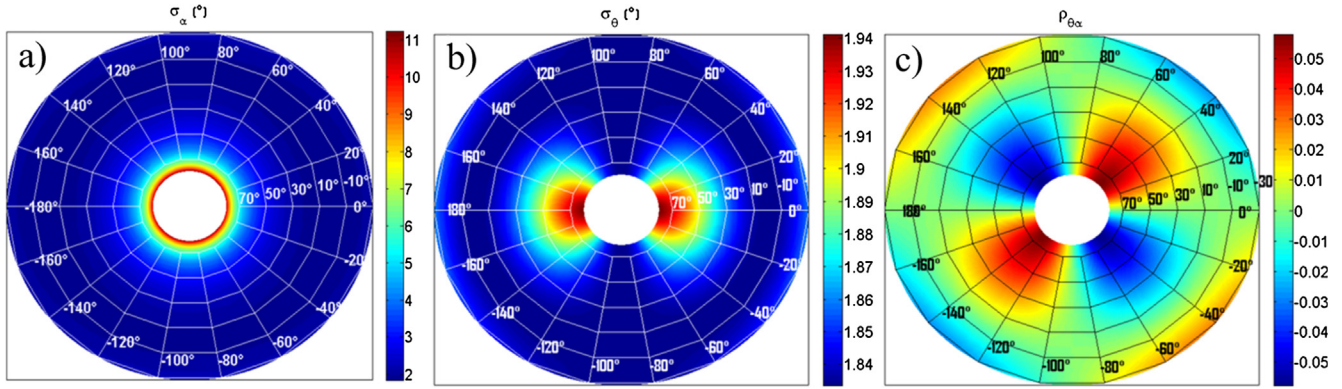
Fig. 7. Results of the calculation of the CRB for the geometry of the "Cyclope" and $\sigma_\tau = 64$ μs. (a) Lower bound of the standard deviation of the azimuth estimation α. (b) Lower bound of the standard deviation of the elevation estimation θ. (c) Coefficient of correlation between elevation and azimuth.
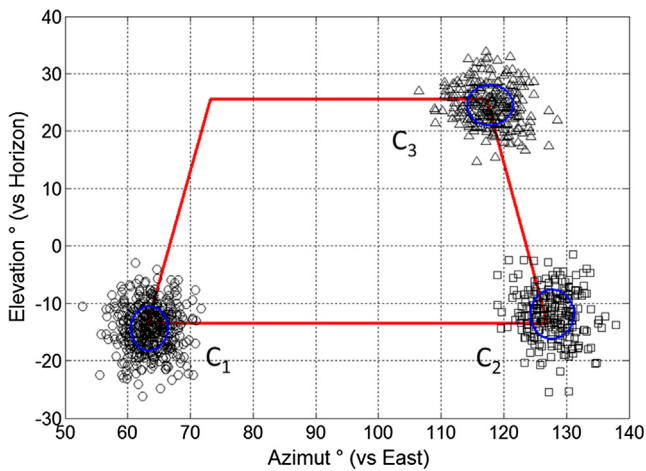
Fig. 8. Estimations of the azimuth and elevation of the VEMCO source at 3 corners of the FAKIR reef. Corner C4 was not included because the divers had to start their ascent. In black, the location of 300 emissions per corner, in blue the CRB ellipse of error, in red the perimeter of the FAKIR reef. (For interpretation of the references to color in this figure legend, the reader is referred to the web version of this article.)

and 10.4 m at 200 m. Numerical simulations not shown here, suggested that the near field assumption was valid within a volume made by the array of the hydrophones enlarged of approximatively 1 m in each dimension. Outside this quite limited volume the far field assumption was met. Inside this volume the position of the sources were defined by their three geometric coordinates and the accuracy was ranging from 0.2 m at the center of the volume to 0.5 m at the border.

4. Second processing stage: Mapping the BIB using the BISs emitted over a significant period of time

A coastal environment can generate more than 50 BISs per second (see Section 5.1). Using recordings of significant duration allows collecting a large number of BISs, each of which can be processed according to the first processing stage for detection and localization. A time series is generated consisting of detection dates, azimuths, elevations and features of the BIS (here SPL_{rms} and $SPL_{peak-to-peak}$). This time series is the raw material used to generate the BIB maps.

The primitive space of mapping is the spherical space, where the BIB is mapped as a function of azimuth and elevation. We propose to refer to this generic representation as the panoramic map (Fig. 9, plots P_1 and P_2). Assuming an *a priori* knowledge of the

surface over which the sources of BIB are distributed, their position can be assessed by intersecting the direction of arrival of the sound {azimuth, elevation} with this surface. Consequently, this allows obtaining well-adapted and specific representations.

Here, we developed two specific map representations. The first one referred to as the sentinel surface map (plot P_3, Fig. 9), focusses on a known surface facing the hydrophone array. The second one, referred to as the seafloor map (plot P_4, Fig. 9) represents a map of the BIB on the seafloor by taking advantage of the sea surface echo of the BISs. In the panoramic map, the number of BISs per unit of time and unit of solid angle (No Imp s^{-1} srad^{-1}) and SPL (rms, peak-to-peak, dB re 1 μPa) are mapped. For the sentinel surface map and the sea floor map, the number of BISs per unit of time and unit of area (No Imp s^{-1} m^{-2}) and SL (rms, peak-to-peak, dB re. 1 μPa at 1 m) are mapped.

4.1. The panoramic map representation

In the case for which we do not have *a priori* information on the surface emitting the BISs, we suggest a generic panoramic map representation (plot P_1, Fig. 9). A sphere is defined around the hydrophone array. The surface of this sphere is discretized into small elementary pixels P corresponding to an azimuth range of [$\alpha_0-d\alpha/2$, $\alpha_0 + d\alpha/2$] and an elevation range of [$\theta_0-d\theta/2$, $\theta_0 + d\theta/2$]. Each pixel defines an elementary cone of known solid angle for which, from the global time series, we search for the directions of arrival of the BISs that belong to this cone. From these selected BISs, we can evaluate the number of BISs per unit of time, as well as the statistical distribution of the SPL (i.e., probability density function, mean, median, percentiles, etc.). We then obtain maps of the number of BISs per unit of time and unit of solid angle as well as the moments of the statistical distributions of the SPL as a function of the central azimuth and the central elevation of the pixels. To finalize the imagery, the maps of the acoustic properties are draped onto the surface of the sphere thus providing the panoramic map representation. To favor understanding, we transposed the spherical surface on a flat support (plot P_2, Fig. 9). On the final planar representation, the azimuth is found on the horizontal axis and the elevation on the vertical axis (Fig. 9, plot P_2, Figs. 10–13 for real data examples).

4.2. The sentinel surface map representation

Here, we assume that the BISs are emitted on a surface S of known distance and orientation from the array of hydrophones. For each elementary pixel of the sphere representing a range of azimuths and elevations (Fig. 9, plot P_3), we can associate an
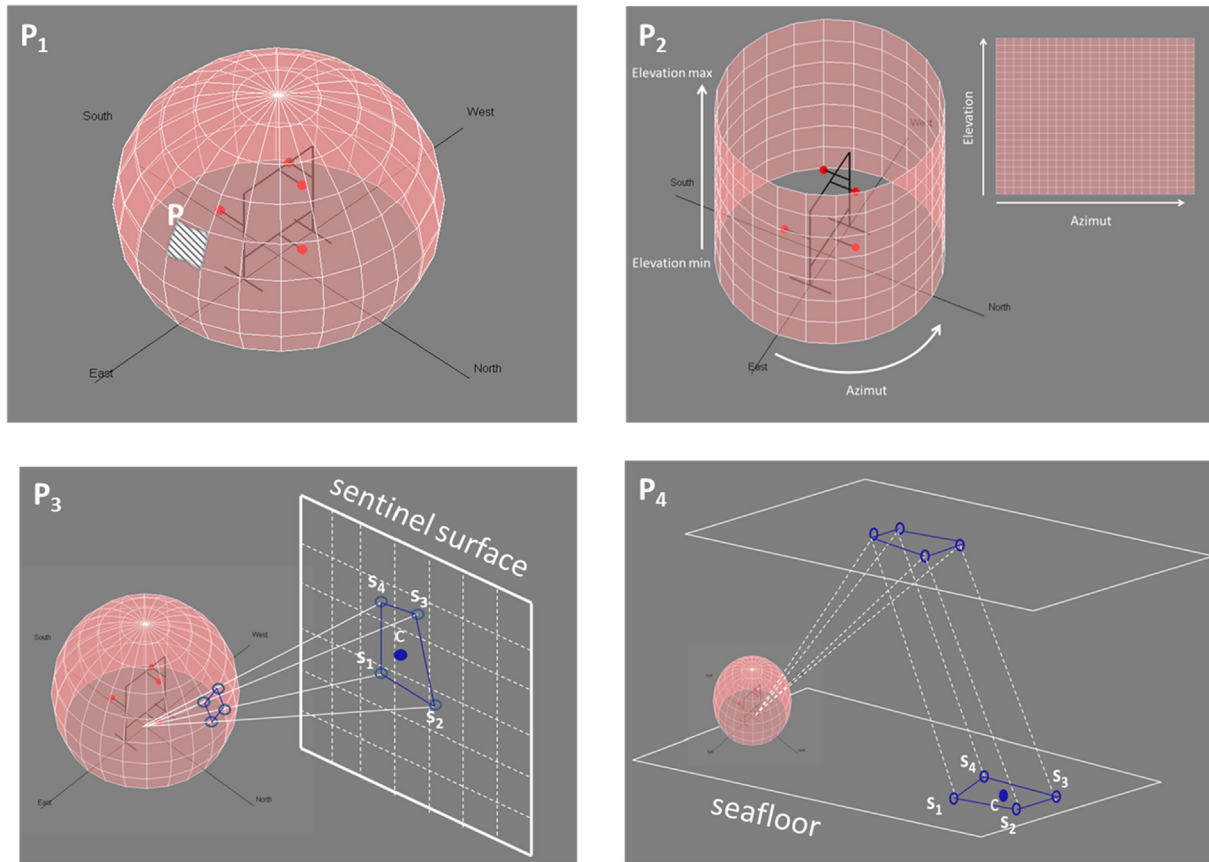
Fig. 9. The 3 types of representations of the map of the BIB. Plots P_1 and P_2: Panoramic map representation in a spherical view (P_1) and in a plane view (P_2), P_3: Sentinel surface map representation, P_4: Seafloor map using echoes from the surface.

elementary surface projected onto S. This surface is a quadrilateral, centered on c and vertex $\{s_1, s_2, s_3, s_4\}$. The position of the center c, the vertex and the area of the quadrilateral can be calculated from the geometric considerations set out in Appendix C. The acoustic descriptors associated with the elementary pixel on the sphere are then associated to the center c on the surface S. Two new descriptors can then be calculated: (i) the SL (dB re. μPa at 1 m) from the distance between c and the recording array and (ii) the number of BISs emitted per unit of time and area around c from the area of the quadrilateral $\{s_1, s_2, s_3, s_4\}$.

4.3. The seafloor map representation

Here, we assume that the BISs are emitted near the seafloor. Due to the roughness of the seabed or to obstacles, the direct path between the source and the recording array can be attenuated or masked. Therefore, the use the echoes reflected on the surface may be of advantage, as they are not be masked. Furthermore, the surface echo of a source located on the seafloor can be seen as the measurement of a virtual hydrophone above the surface, symmetric to the real one. This virtual hydrophone increases the size of the array along the vertical axis and allows to estimate the range of the source [58] in addition to its depth and azimuth. Consequently, the absolute positions of the sources located on the seafloor are available. At each elementary pixel of the sphere representing a range of azimuth and elevation, we can associate an elementary surface projected on the seafloor. This surface is a quadrilateral centered on c and vertex $\{s_1, s_2, s_3, s_4\}$ (plot P_4, Fig. 9). If the water depth is known, the position of the center c, the vertex and the area of the quadrilateral can be calculated from

the geometrical considerations set out in Appendix C. The acoustic descriptors associated with the elementary pixel on the sphere are then associated to the center c on the seabed. By doing so, two new descriptors can be calculated: (i) the SL (dB re. μPa at 1 m) from the length of the surface-reflected path between c and the recording array and (ii) the BIS density emitted per unit of time and of area around c from the area of the quadrilateral $\{s_1, s_2, s_3, s_4\}$.

### 4.4. Synthesis of the parameters of the mapping process

Table 2 summarizes the essential settings of the processing chain and the values used for the results presented in part 4.

5. Application to the Prado2015 campaign

5.1. Panoramic maps of the FAKIR and ROCKS reefs

During 10 h of acoustic recordings (29/09/2015 at 21: 00 to 30/09/2015 at 07:00) at the FAKIR reef, the recording array "Cyclope" detected 1,955,822 BISs on channel A, i.e. 54 BISs/second, and localized 430,267 BISs corresponding to 8 BISs/second, or 22% of the overall detected BISs.

Fig. 10 shows the panoramic map of the number of BISs emitted per hour in a cone of 2° by 2° as a function of elevation and azimuth for the FAKIR reef, whereas Fig. 11 presents the panoramic map of the 90th centile of the SPL_{rms}. The distribution of the BISs and their SPLs were not homogeneous over space. The highest densities of BISs were concentrated in a ring (ring r, Fig. 10 or Fig. 11) with elevations ranging between −7° to +7°. These BISs, near the
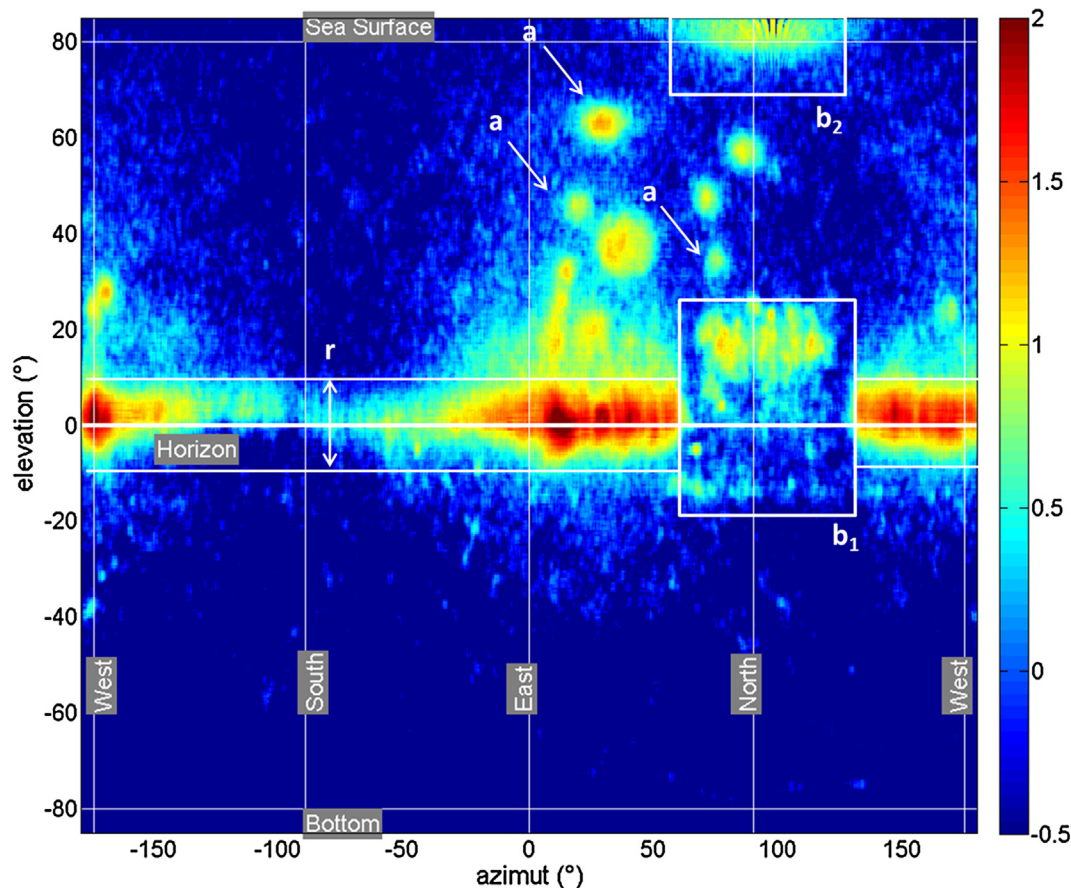
Fig. 10. Panoramic map of the number of BISs emitted per hour in a cone of 2° by 2° in elevation and azimuth for the FAKIR reef. Logarithmic color map (blue color for 1 BIS per hour in a cone of 2° by 2°, yellow for 10 BIS per hour in a cone of 2° by 2°, red for 100 BIS per hour in a cone of 2° by 2°), r : elevations between −7° and +7° comprising the BISs coming from the horizon, box b_1: Angular window of the FAKIR reef located northward of the "Cyclope" array, box b_2: angular window above the FAKIR reef corresponding the BISs emitted at the top of the FAKIR and reflected at the surface. Arrows a: example of local maxima of the number of BIS per hour in a cone of 2° by 2° with positive elevation corresponding to BISs emitted by distant reefs and reflected at the surface. (For interpretation of the references to color in this figure legend, the reader is referred to the web version of this article.)

horizontal direction, were produced by distant reefs of village n°6 (Fig. 1). This ring comprised 244,875 pulses, i.e. 56% of the localized BISs. This horizontal area of high density of BISs has moderate $SPLs_{rms}$ due to the great distance of the sources and potential masking by the bathymetry or other artificial reefs. This area of high BIS density showed a density decrease for azimuth between 66° and 127° (box b_1, Figs. 10 and 11) coinciding with the highest SPL_{rms} values. This region (boxcar b_1) corresponds to the angular acoustic "fingerprint" of the front side of the FAKIR facing the hydrophone array at 3 m. 46,311 BISs were directly emitted by the module (i.e. 10.7% of the localized BISs) for elevations between −20° and +25° and with SPL_{rms} values of the 90th percentile of the order of 130 dB re 1 μPa and more. On top of boxcar b_1 is boxcar b_2 (Figs. 10 and 11) with the same azimuthal range but with elevations near the vertical axis (i.e., >75°). Boxcar b_2 corresponds to the echoes of the BISs emitted at the top of the FAKIR reef and reflected at the sea surface. Around 11 local maxima of BIS density or SPL_{rms} appear at positive (>10°) elevations (arrows a, Figs. 10 and 11). These local maxima correspond to sea surface echoes of BISs emitted at the top of other distant reefs. This is highlighted by the fact that the azimuth of theses local maxima coincides with local maxima in the ring r, which correspond to the direct path of the BISs of distant reefs.

Fig. 12 shows the panoramic map of the number of BISs emitted per hour in a cone of 2° by 2° in elevation and azimuth for the ROCKS reef, whereas Fig. 13 presents the panoramic map of the

90th percentile of the SPL_{rms}. The panoramic maps of the ROCKS reef follow the same general patterns as the ones of the FAKIR reef. The horizontal ring concentrates the highest density with several local maxima (arrows c, Fig. 12). Each local maximum corresponds to a distant reef. To confirm this, for each azimuth angle we summed the number of BISs with elevations within −7° and +7° to obtain a density of horizontal BISs as a function of the azimuth. We then created a polar-plot of this density on top of the side-scan sonar map of the reef system. The polar-plot of the density curve was centered on the ROCKS reef (Fig. 14). The connection lines between the origin (ROCKS reef) and the local maxima of the density curve of the polar plot (Fig. 14, black arrows) follow three regimes. For the angular sector A (Fig. 14), the curve does not present local maxima and the far reefs are not detected; here the close ROCKS reef masks the more distant reefs. The radius from ROCKS oriented toward the direction of a local maxima, (Fig. 14, numbers 4–16) always intercept a reef within a 3-m accuracy, which is coherent with the angular resolution of the here-described process (5 m at a distance of 100 m) and the accuracy of the towed side-scan sonar (2 m). For directions that always intercept a reef within 10 m (Fig. 14, radius 1–3) the accuracy is degraded because of the partial masking of the closest ROCKS reef. The local maxima of the density curve coincide with distant modules of the artificial reef system. The ROCKS and FAKIR reefs differ in the boxcar b_1 representing the angular "fingerprint" of the reef. For the ROCKS reef, the density of BISs within boxcar b_1 (Fig. 12) was weak (~10 times
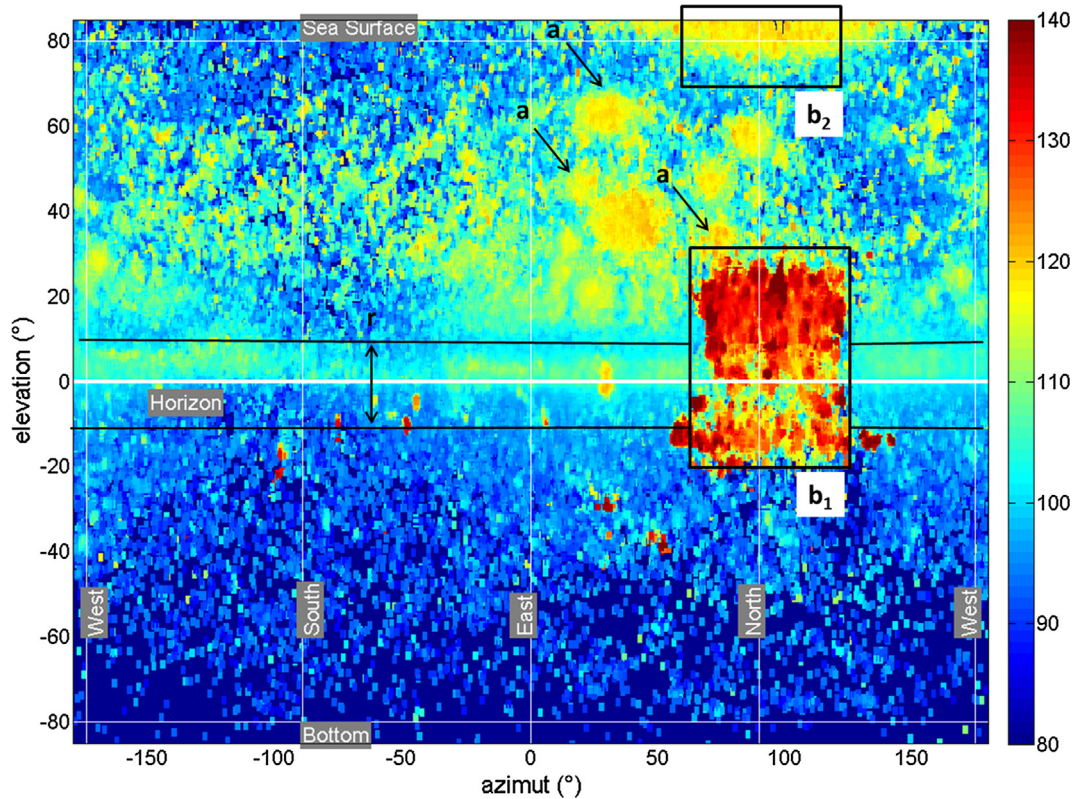
Fig. 11. Panoramic map of the 90th centile of the SPL$_{rms}$ (dB re1μPa) of the BISs in a cone of 2° by 2° in elevation and azimuth for the FAKIR reef. r: elevations between −7° and +7° comprising the BISs coming from the horizon, box b$_1$: Angular window of the FAKIR reef located northward of the "Cyclope" array, box b$_2$: angular window above the FAKIR reef corresponding the BISs emitted at the top of the FAKIR and reflected at the surface. Arrows a: example of a local maxima of the 90th centile of the SPL$_{rms}$ in a cone of 2° by 2° with positive elevation corresponding to the BISs emitted by distant reefs and reflected at the surface.

less that the one of FAKIR). We hypothesize that the many rocks composing the ROCKS reef mask the direct path propagation between the BISs and the array. On the contrary, the density is high within the boxcar b$_2$, corresponding to echoes of the BISs emanating from the ROCKS reef and reflecting on the sea surface. These surface-reflected echoes are less subject to masking by the rocks constituting the ROCKS reef. The small number of BISs contained within box b1 has the highest SPL$_{rms}$ (box b1, Fig. 13).

Finally, the panoramic maps of the FAKIR and ROCKS reefs indicate that the front side of the FAKIR reef is a good candidate for the sentinel surface map representation, whereas the top side and the surroundings of the ROCKS reef are appropriate candidates for the seafloor map representation using surface echoes.

5.2. Sentinel surface map of the front side of the FAKIR reef

Fig. 15 presents the sentinel surface map of the number of BISs per hour and square meter at the front side of the FAKIR reef, while Fig. 16 presents the 90th percentile of the SL (dB re 1 μPa at 1 m). Density and SL match the geometry of the reef and show specific biophonic modulations. The density of BISs is not equally distributed over the surface of the reef. "Hot-" and "cold-" spots are spread over the surface. Details clearly appear at a scale of 30 cm. This validates the results of the resolution/accuracy exposed in Section 3.3. Density was poor at the borders of the reef, particularly along the vertical stakes as well as the lower part of the module (Fig. 15). In contrast, the upper level of the reef showed high BIS density, in particular within the cavity structures of the module (Fig. 15). The distribution of the 90th percentile of the SL follows exactly the same pattern as the density. The SL of the "hotspots" ranged between 145 and 150 dB re 1 μPa at 1 m, which

is in agreement with Lossent et al. [59], who measured 147 dB re 1 μPa at 1 m.

Under the assumption of transmission loss [60] equal to

$$TL(r) = 10log_{10}\left(\frac{r}{2h}\right) + 20log_{10}(2h) \qquad (6)$$

with h representing the water depth, the range of the BIB of the FAKIR reef was 100 m with a SNR of 10 dB, 503 m with a SNR of 3 dB, 1000 m with a SNR of 0 dB.

5.3. Seafloor map using the surface echoes of the BISs of the neighborhood of the ROCKS reef

Seafloor maps were built based on the measurements obtained from the hydrophone array located at the ROCKS reef. All the BISs with an elevation greater than 10° (Fig. 12, area A$_1$) were considered as surface echoes and were back-propagated on the seafloor. Fig. 17 presents the map of the number of BISs per hour and 100 m^2. The map of the 90th percentile of the SL is given in Fig. 18. The BIB was not homogenous within the 300-m radius around the array. Hot-spots appeared around each artificial reef in a radius of 200 m around the array. The density decreased with the distance to the array. One cause may be the attenuation of the BISs' SPL due to propagation resulting in smaller SNR values. Compared to the side-scan sonar map, the resolution of the acoustic map was good below 75 m around the measurement point and slowly degraded from 75 m to 200 m. ROCKS reefs were detected and localized up to 200 m. Furthermore, the results obtained on the dead matte and on the seagrass surrounding village n° 6 illustrate how the here-proposed method can be transposed to natural environments with a well-defined frontier between the dead matte
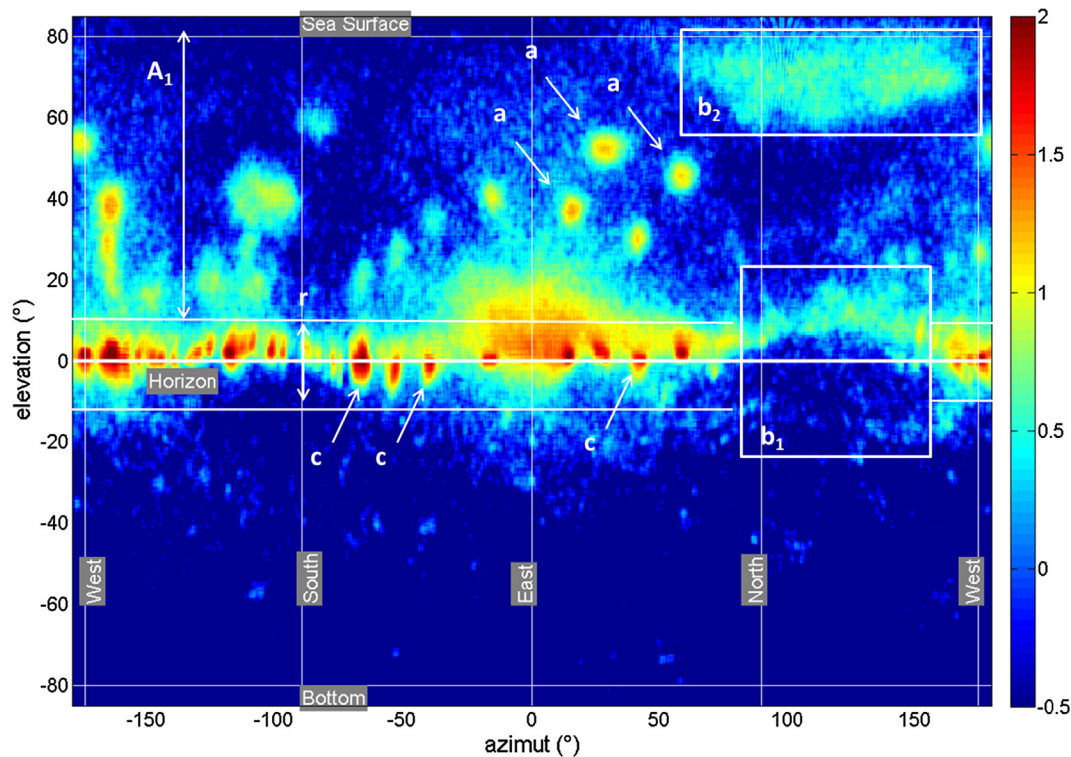
Fig. 12. Panoramic map of the number of BISs emitted per hour in a cone of 2° by 2° in elevation and azimuth for the ROCKS reef. Logarithmic color map (0-blue => 1 BIS per hour in a cone of 2° by 2°, 1-yellow => 10 BISs per hour in a cone of 2° by 2°, 2-red => 100 BISs per hour in a cone of 2° by 2°), ring r: elevations between −7° and +7° comprising the BISs coming from the horizon with local maxima (arrows c) associated to distant reefs, box b_1: Angular window of the ROCKS reef located northward of the "Cyclope" array, box b_2: angular window above the ROCKS reef corresponding the BISs emitted at the top of the ROCKS and reflected at the surface. Arrows a: example of a local maximum of the number of BISs per hour in a cone of 2° by 2° with positive elevation corresponding to BISs emitted by distant reefs and reflected at the surface. (For interpretation of the references to color in this figure legend, the reader is referred to the web version of this article.)
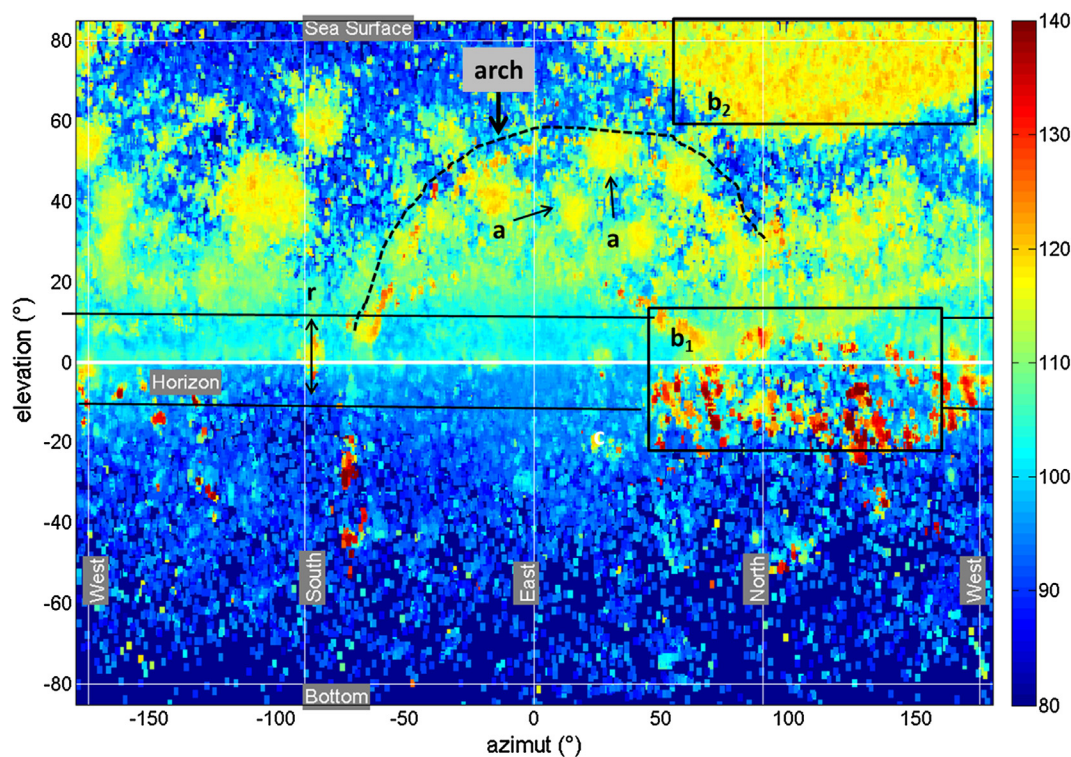
Fig. 13. Panoramic Map of the 90th centile of the SPL_{rms} (dB re1 µPa) of the BISs in a cone of 2° by 2° in elevation and azimuth from the ROCKS reef. r: elevations between −7° and +7° comprising the BISs coming from the horizon, box b_1: Angular window of the ROCKS reef located northward of the "Cyclope" array, box b_2: angular window above the ROCKS reef corresponding the BISs emitted at the top of the ROCKS and reflected at the surface. Arrows a: example of a local maximum of the 90th percentile of the SPL_{rms} in a cone of 2° by 2° with positive elevation corresponding to BISs emitted by distant reefs and reflected at the surface. The arch represented by the dotted black line corresponds to loud bathymetric sonar emissions of a passing boat.

Table 2
Synthesis of the settings of the processing chain.

Settings	Bloc in Fig. 5	Value
Bandpass filter	C_1	[1500 Hz, 70,000 Hz]
N_{int}: Size of integration for envelope calculation	C_3	64 samples
Q_1, Q_2 percentiles for the calculation of the ANL	C_4	Q1 = 0.2, Q2 = 0.5
Pfa for CFAR	C_5	10^{-6}
Neutralization time after detection	B_3	2 ms
Path difference accuracy threshold	B_6, B_7, B_8, B_9	0.05 m
Discretization of the search space of the azimuths and elevations of the source	B_6	Azimuth = −180°:0.1°:180°
		Elevation = −90°:0.1°:90°
Discretization of the search space of the x, y, z of the source	B_8	X = −10 m :0.2 m :10 m
		Y = 10 m:0.2 m:10 m
		Z = 10 m:0.2 m:10 m
Discretization of BIB maps[*]	Generic panoramic mode	720 × 360 pixels
		720 central azimuths = −180°:0.5°:180°
		360 central elevations = −90°:0.5°:90°
		Pixel width in elevation = 2°
		Pixel width in azimuth = 2°

[*] The step and width of the discretization of the azimuth and elevation angles are consistent with the angular resolution of the order of 3° of the "Cyclope" recording array.
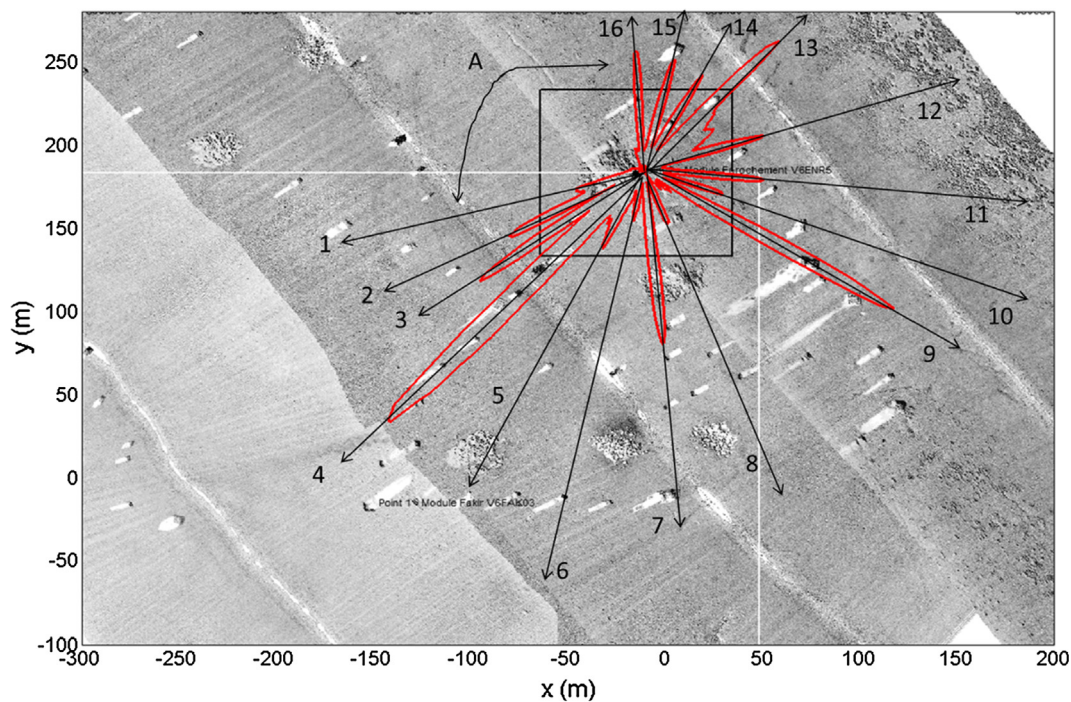
Fig. 14. ROCKS Polarplot (centered on the ROCKS reef) of the relative density of horizontal BISs superposed on the side-scan sonar map. Each black arrow is a line passing by the center of the array and a local maximum of the density curve. A is the north-east angular sector where masking by the close ROCKS reef holds on.

and the living seagrass. As illustrated in Fig. 17, the density was very poor in the dead matte, while it was high within the *Posidonia oceanica* meadow (area A1, Fig. 17). The areas of high SL coincided with the area of high density. The ROCKS reefs appear to host the loudest BIB compared to the other reef types as well as the *Posidonia oceanica* meadow, although the differences remain below 13 dB.

6. Discussion

Recent developments in soundscape ecology highlighted the need to link a sound emission with its position and to estimate the density (number of emissions per unit of surface) rather than number of BISs only [19,20].

The main contribution of our study was to describe and illustrate the 3D mapping of the BIB using a simple operational system (cost efficient, ease of use). We propose a novel, straightforward methodology that produces acoustic maps of the BIB from a compact 2 m × 2 m × 2 m array of 4 hydrophones at both small and large scales. The maps are based on individually detected BISs localized in azimuth and elevation using the TOAD between pairs of hydrophones. As the production of the BIB is sustained (54 BISs/s in this study, [61,62]), a recording session of several hours makes it possible to collect BISs coming from all possible emission sites. The extraction of acoustic features from the detected BISs allows building acoustic maps at different spatial scales.

The here-proposed work lies within the framework of tool development for underwater eco-acoustic studies. To our knowledge, three studies [11,43,48] used operational instrumentation and suggested processing chains to describe the directionality (azimuth) of the BIB of coastal ecosystems. In these three studies, advanced adaptive or non-adaptive beam forming algorithms, well-suited for planar and spherical waves, were fed with the spectral coherence functions between sensors. This allows limiting the
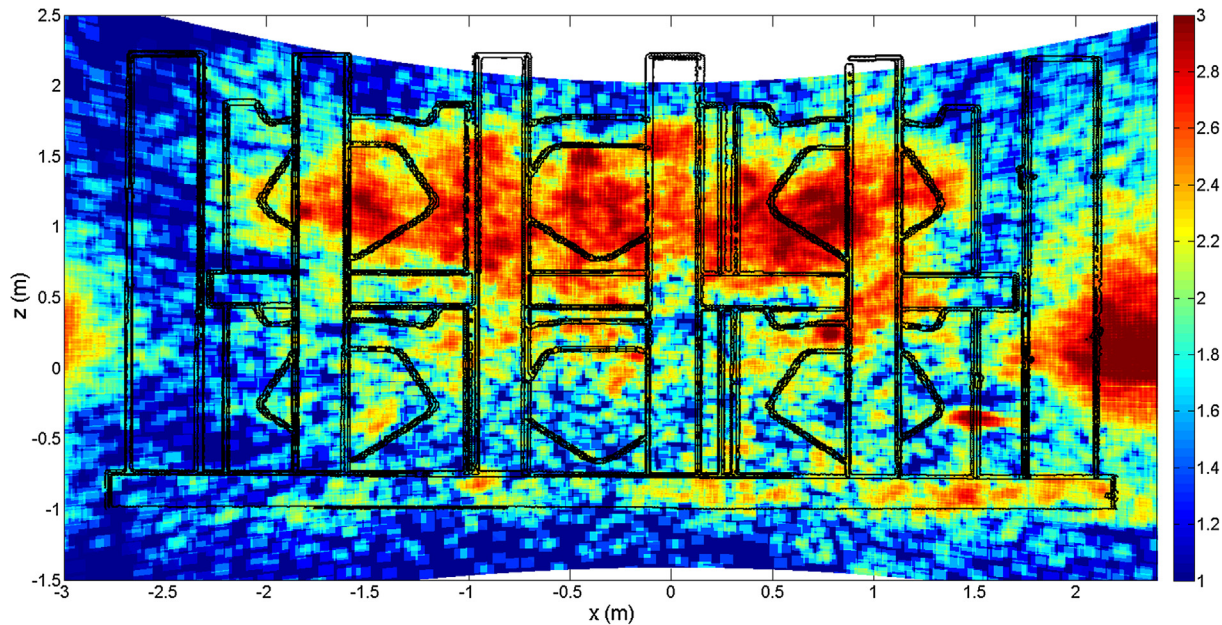
Fig. 15. Sentinel surface map of the number of BISs per hour and m² on the front side of the FAKIR reef, logarithmic color scale (1-blue => 10 BISs per hour and m², 2-green => 100 BISs per hour and m², 3-red => 1000 BISs per hour and m²), black thin line: contour of the FAKIR reef (source E. Medioni, City of Marseille). (For interpretation of the references to color in this figure legend, the reader is referred to the web version of this article.)
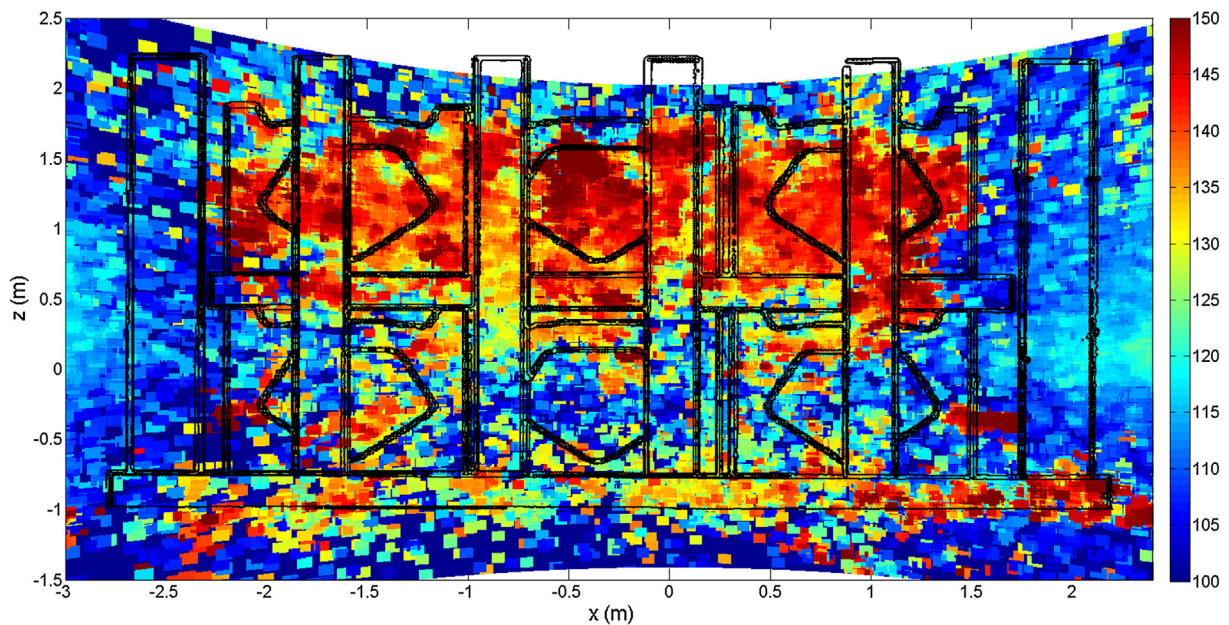

Fig. 16. Sentinel surface map of the SL(dB re 1 μPa at 1 m) on the front side of the FAKIR reef, black thin line: contour of the FAKIR reef (source E. Medioni, City of Marseille).

number of sensors by using the large bandwidth of the coherent signals from one sensor to another. As the spectral coherence function is built from an FFT to compute the azimuth of the wave, the spectral coherence function between sensors integrates simultaneously the direct path and a series of echoes, with time of arrivals falling within the FFT window. The set of echoes with their own positive or negative elevations emanate from the reverberation. As long as we consider hydrophones distributed on the same horizontal plane, this reverberation is very similar from one hydrophone to another, in particular if the inter-sensor distance is small compared to the distance between the recording array and the source. In this case, the reverberation does not cause the spectral coherence function to collapse. For the localization and a mapping in three dimensions, it is necessary to arrange the

hydrophones at different depths. In this configuration, the reverberation between two hydrophones at different depths varies, even if they are close to each other. In this case, the coherence function collapses and the solutions proposed in Ferguson and Cleary, Miklovic and Bird and Freeman et al. [11,43,48] are no longer appropriate. D'Spain and Batchelor [49] showed a successful characterization of the vertical directionality of BIB from a planar antenna of 6 m height and 0.6 m width, comprising 131 hydrophones. The large number of sensors makes it possible to directly apply classical or adaptive tracking techniques even in the presence of reverberation. However, this type of system is costly and difficult to deploy. To succeed in mapping the BIB in 3D with only 4 hydrophones, we suggested a new approach, which consists in working only on individual BISs that emerge from the background
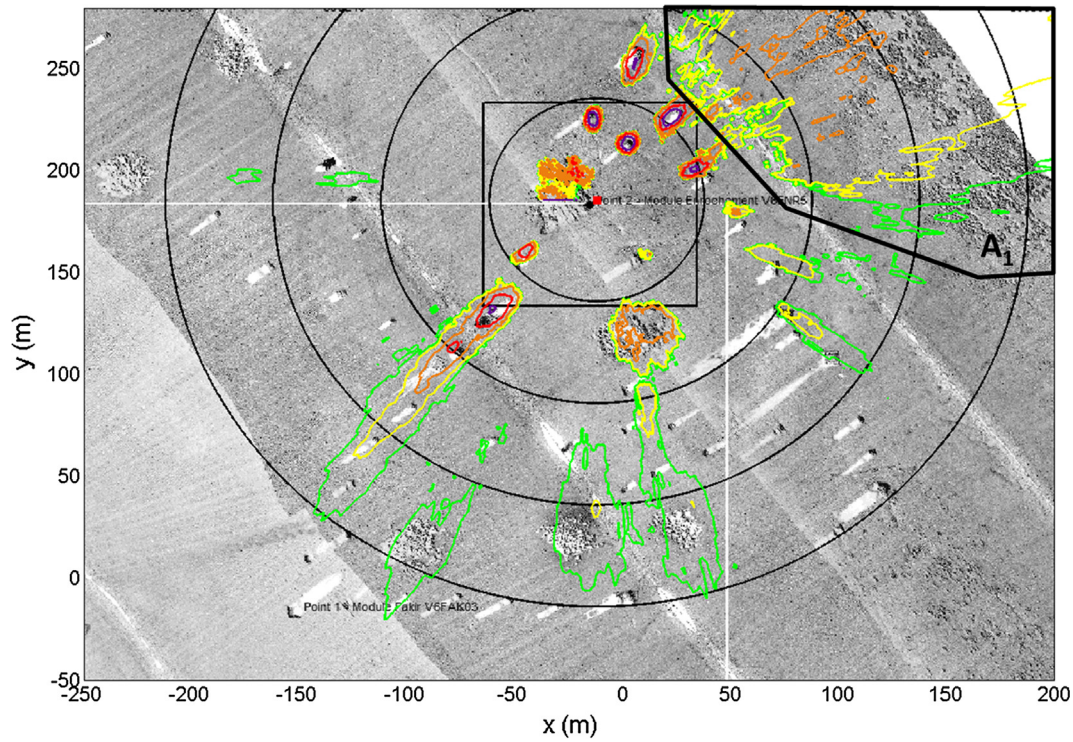
Fig. 17. Seafloor map of the number of BISs per hour and per 100 m^2 of the neighborhood of the ROCKS reef. Grey scale background layer: side-scan sonar map, black circles: 50 m, 100 m, 150 m and 200 m radius centered on the array, black area A$_1$: *Posidonia oceanica* meadow. Colored lines: iso-contour of the number of BISs per hour and per 100 m^2 – green = 280 BISs per hour and per 100 m^2, yellow = 560 BISs per hour and per 100 m^2, orange = 1120 BISs per hour and per 100 m^2, red = 2240 BISs per hour and 100 m^2, purple = 4480 BISs per hour and per 100 m^2. (For interpretation of the references to color in this figure legend, the reader is referred to the web version of this article.)
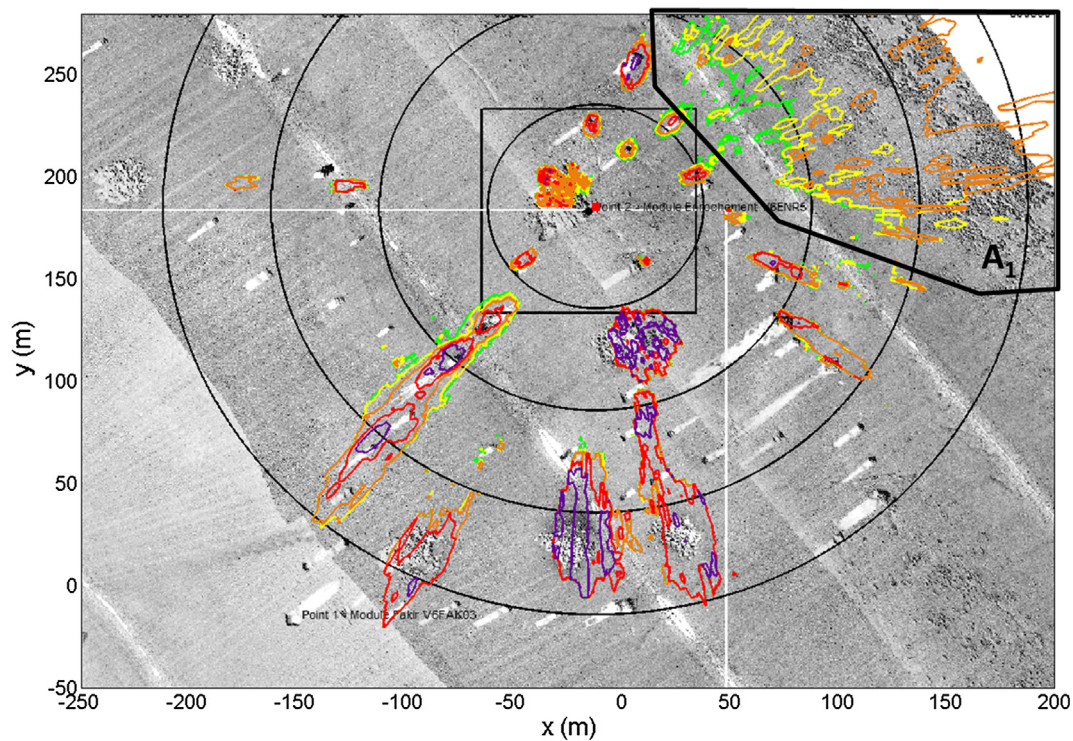
Fig. 18. Seafloor map of the 90th centile of the SL (dB re 1 μPa at 1 m) of the neighborhood of the ROCKS reef. Grey scale background layer: side-scan sonar map, black circles: 50 m, 100 m, 150 m and 200 m radius centered on the array, black area A$_1$: *Posidonia oceanica* meadow. Colored lines: iso-contour of the 90th centile of the SL (dB re 1 μPa at1m) – green = 132 dB, yellow = 135 dB, orange = 138 dB, red = 142 dB, purple = 145 dB. (For interpretation of the references to color in this figure legend, the reader is referred to the web version of this article.)

Table 3
Summary of the performance of the methods developed.

Method	Configuration of the application	Mapping range	Mapping resolution	Density unit
Panoramic Map	All benthic sources	~500 m	3° in elevation and azimuth, 15 m at a distance of 300 m	Number of BISs per unit of time and unit of solid angle
Surface Sentinel Map	Sources on a known vertical surface	~5 m	0.2 m in the mapping range	Number of BISs per unit of time and unit of surface
SeaFloor Map	Sources on the seafloor	~200 m	10 m in the mapping range	Number of BISs per unit of time and unit of surface

ambient noise. We can therefore take advantage of the large bandwidth naturally present in these transient sounds [63] in order to estimate their TOA. The TOA were based on the rising edge of the BIS, i.e., the first instant at which the sound level of the sound exceeds the detection threshold. This rising edge informs about a single arrival from a direct path or a surface reflected path. By working with rising edges, the influence of the reverberation can be avoided. This allows to realize localization in azimuth and elevation of the BISs. The outputs of the here-proposed method are maps of the density of BISs and of their acoustic features. For the panoramic map, the density of BIB is the number of BISs per unit of time and per unit of solid angle. If some a priori knowledge is available about the location of the surface where the benthic invertebrates are situated, the azimuth and elevation may be converted in absolute 3D positions. For the sentinel surface map and the seafloor map the density of the BIB is the number of BISs per unit of time and surface. In this study, we illustrated the mapping of two acoustic features, the SPL$_{rms}$ and SL$_{peak-to-peak}$, but any other measurable BIS feature (peak frequency, duration, etc.) can be mapped as well. The mapping process if fully quantitative and allows comparisons between areas, surfaces, objects, etc. Furthermore, the sentinel surface map allows to follow benthic invertebrate activity at small scales with a high accuracy within a defined area or volume (i.e., here the artificial reefs). It therefore represents a means to identify and follow bioacoustics hotspots over space and time. The seafloor map presents the features projected on the seafloor, providing a large-scale map of the benthic invertebrate activity and also allowing to assess detection or hearing ranges. Together, these represent key parameters, usually missing in eco-acoustics surveys.

Another advantage of the here-proposed localization method is its accuracy and mapping resolution. The results using *in situ* measurements of known active emission locations matched the theoretical framework based on CRB. The angular accuracy and resolution were 3° in azimuth and elevation, implying a spatial accuracy and resolution equal to 0.15 m for a source located at 3 m of a recording array, 0.5 m at 10 m, 2.6 m at 50 m, 5.2 m at 100 m and 10.4 m at 200 m (see Table 3). This high accuracy, particularly at small ranges, allows identifying acoustic patterns also over small spatial scales and track sound sources. This was clearly illustrated in the sentinel surface map of the FAKIR reef that perfectly matched the geometry and structure of the reef. This not only confirms the accuracy and resolution of the here-proposed method, but also emphasizes patterns of acoustic map linked to local benthic activity. This may have implications if such acoustic hot-spots are associated to specific species or behaviors. Combined to the metrics that can be calculated (e.g., density, SL), such activities/behaviors can be quantified and used to assess ecologically-relevant processes (e.g., quantification of grazing activity in sea urchins).

The here-proposed 3D mapping method also allows direct comparisons. The panoramic maps of BIB densities and SPL$_{rms}$ for instance, highlighted differences between the two artificial reef types but also shared patterns that can be implemented in monitoring surveys and compared to other data such as biomass, diversity etc. For both, the FAKIR and ROCKS reef, the BIB was not uniform in space, but highly directional. Only ~10% of the BISs were emanated by the nearest FAKIR or ROCKS reef. The panoramic maps of the two modules differed. While the side of the FAKIR reef facing the hydrophone array was clearly visible, it was almost absent in the ROCKS reef. However, because the BISs echoes from the sea-surface above the ROCKS reef were numerous, the difference observed may not result from a smaller benthic activity of the ROCKS reef compared to the FAKIR, but rather indicate that the rocks composing the reef mask the direct horizontal propagation path.

Using the same compact hydrophone array system, we were also able to create large-scale maps, referred to as seafloor maps using the surface echoes of the BISs of distant reefs. The seafloor map matched the side-scan sonar map. The sea-surface reflected echoes that appeared as local maxima in the density map at elevations greater than 7° corresponded to distant modules on the side-scan sonar map. The maxima of the sea-surface reflected echoes used for the seafloor map also coincided with the local azimuth maxima of the horizontal ring with an elevation between −7° to +7° in the panoramic map. This ring concentrated the highest density of BISs i.e., almost 60% of all detected BISs and the retro-propagation of the observed maxima to their sources, revealed that they were indicative of distant soniferous reefs. The BIB of reefs at up to 200 m distance could successfully be located and mapped using the seafloor map method with an accuracy equal to 15 m, which further confirms our prediction of accuracy and resolution. The seafloor map indicates differences in density and SL between different reef types. However, to avoid misinterpretation, direct comparisons should only be conducted between reefs located approximately at the same distance from the array. Besides providing a detailed large-scale acoustic map, the seafloor map approach also allows to differentiate between natural habitats. The BIB of the dead matte was poor and weak compared to the rich and loud BIB of the *Posidonia oceanica* meadow. A comparison between the BIB of the *Posidonia oceanica* meadow and the BIB of the artificial reefs, allows to identify the artificial reefs that reproduce a number of BIS per unit of time and unit of surface equivalent to the natural one and those reefs that produce more or less than the natural BIB.

7. Conclusions

The mapping processes presented in this study demonstrated that the BIB is highly directive and coming from localized acoustic hot- spots including artificial reefs or natural habitats. Our results also highlight the potential of this compact, easily replicable system and its derived acoustic maps for eco-acoustics or ecological applications. The full understanding of the BIB to diagnose which reefs are the best hosts for marine fauna, the most efficient ones, or to describe how the reefs are connected with their surrounding natural environments requires a directive multi-hydrophone hearing and a mapping process.

Our results also suggest that passive acoustic monitoring with directional hearing and mapping is appropriate to survey the efficiency of ecological restoration actions such as artificial reef deployments or to follow the settlement of the fauna on newly introduced structures such as marine renewable energy devices.

This work represents a first and promising step towards the use of acoustic maps to answer ecologically-relevant questions at local

spatial scales. An additional key development of the here-proposed method would be to adapt it to the biophony of fishes using a larger 10 m × 10 m × 10 m four hydrophones array to account for the lower frequencies of fish sounds. Knowledge on spatio-temporal activity of marine species and entire communities, home ranges and acoustic spaces of fish species, movements, etc. is still sparse but ecologically critical. Advances in the here-proposed method will help to study these issues and fill some of these gaps.

Acknowledgments

Appendix A. Algorithm for the Constant false alarm Rate (CFAR) detection of individual pulses

Let $s_1(n)$ be the raw measurement at time n. T_e of one channel of the 4-hydrophones array. Firstly, $s_1(n)$ is filtered by a bandpass Butterworth filter of 4th order to produce $s_2(n)$. The lower cutoff frequency is 1500 Hz and the higher cutoff frequency is 70,000 Hz (C1, Fig. 5).

Then the energy of $s_2(n)$ over the duration T = N_{int}. Te is computed by (C2 and C3, Fig. 5):

$$u_1 = n - \frac{N_{int}}{2} - 1$$
$$u_2 = n + \frac{N_{int}}{2} \qquad (7)$$
$$E_{S2}(n) = \sum_{u_1}^{u_2} (s_2(n-u))^2$$

$E_{S2}(n)$ is the statistic test T that will be compared to a threshold λ (C6, Fig. 5) to run the detection.

This threshold is based on a Constant False Alarm Rate detector. Let $cdf_T(\alpha)$ be the cumulative distribution function of test T, when the measurements contain noise only, and Pfa the aimed probability of a false alarm, then the threshold of detection is given by:

$$\lambda = cdf_T^{-1}(1 - Pfa) \qquad (8)$$

To compute $cdfT(\alpha)$, we made the assumption that the samples of the noise at different times are independent, identically distributed and following a normal distribution of zero mean and variance equal to ANL (Ambient Noise Level). Under these assumptions, $E_{S2}(n)$ follows a chi-squared distribution with N_{int} degrees of freedom. Its mean is equal to N_{int}. ANL. If N_{int} is higher than 20, then the chi-squared law may be approximate by a Normal law. The two parameters (mean equal to ANL and variance σ^2) are unknown and must be estimated directly from the measurements (C4, Fig. 5).

We follow the method described by Kinda et al. [55]. A 10s-snapshot of $E_{S2}(n)$ is selected and a single ANL law is estimated for each sample in the 10 s interval. The time series of $E_{S2}(n)$ is then ordered and two small quantiles Q1, Q2 are chosen (typical value: Q1 = 0.2, Q2 = 0.4). Let $E(Q_1)$ and $E(Q_2)$ be the value of the energy at these quantiles. Because the quintiles Q_1 and Q_2 are small, we assume that their levels are constituted by background noise only and can be used to infer the two parameters of the normal law:

$$ANL = \frac{erfc^{-1}(2Q_1)E(Q_2) - erfc^{-1}(2Q_2)E(Q_1)}{erfc^{-1}(2Q_1) - erfc^{-1}(2Q_2)} \qquad (9)$$

$$\sigma = \frac{-1}{\sqrt{2}} \frac{E(Q_1) - E(Q_2)}{erfc^{-1}(2Q_1) - erfc^{-1}(2Q_2)} \qquad (10)$$

Then the detection threshold λ is:

$$\lambda = ANL - \sqrt{2}\sigma erfc^{-1}((1 - Pfa)) \qquad (11)$$

Appendix B. Formulation of TOA under the wave-plane hypotheses and derivation of the Cramer Rao Bounds (CRB) for the azimuth and elevation

We assume a 3D recording array consisting of 4 hydrophones arranged at positions {x_i, y_i, z_i}, i ∈ {1,2,3,4}, an acoustic source at large distance generating a plane wave with its direction of arrival defined by its azimuth α_s and its elevation θ_s. For two different sensors of indices i and j, the vector connecting these two sensors is defined by:

$$x_{ji} = [x_j - x_i, y_j - y_i, z_j - z_i] \qquad (13)$$

The direction vector of the wave ensonifying the recording array is defined by:

$$u = [-cos(\theta)cos(\alpha), -cos(\theta)sin(\alpha), -sin(\alpha)] \qquad (14)$$

The difference in the TOA of the incident wave between the sensor j and the sensor i is given by:

$$\tau_{ji} = \tau_i - \tau_j = \frac{-1}{c} < x_{ji}, u > \qquad (15)$$

Where <...> is the scalar product.

Thus:

$$\tau_{ji} = \frac{-1}{c}[(x_j - x_i)cos(\theta)cos(\alpha) + (y_j - y_i)cos(\theta)sin(\alpha) + (z_j - z_i)sin(\theta)] \qquad (16)$$

The Cramer-Rao theorem [57] indicates that for any unbiased estimator of $\{\widehat{\alpha}, \widehat{\theta}\}$ on the basis of TOAD measurements, we have:

$$cov(\widehat{\alpha}, \widehat{\theta}) - I^{-1} \geq 0 \qquad (17)$$

where I is the Fisher information matrix.

Thus, the diagonal terms of I^{-1} are lower bounds of the variance of any unbiased estimator of $\{\widehat{\alpha}, \widehat{\theta}\}$. These lower bounds called "Cramer Rao Bounds" are reached asymptotically by the maximum likelihood estimator.

Under the assumption that the TOAD measurements are corrupted with a Gaussian additive noise of variance σ_τ^2 and independent for two pairs of different hydrophones, then the maximum likelihood estimator consists in minimizing the criterion J_{FF} [57] and the Fisher information matrix is simply written as:

$$I = \frac{1}{\sigma_\tau^2} \begin{bmatrix} \frac{\partial \tau}{\partial \alpha} \\ \frac{\partial \tau}{\partial \theta} \end{bmatrix} \begin{bmatrix} \frac{\partial \tau'}{\partial \alpha} & \frac{\partial \tau'}{\partial \theta} \end{bmatrix} \qquad (18)$$

where τ is a vector column collecting the different TOAD τ_{ij} for i and j between 1 and 4 and i ≠ j.

Appendix C. Details of the geometric calculations for sources located on known sentinel surfaces and on the seafloor via reflected echoes on the surface

Here we provide the elements for calculating the positions of the points and the areas of the surfaces for the specific case of the mapping of BIB coming from known surfaces: a vertical surface and the seabed. For both cases, we have to connect the direction of arrival given by the azimuth and the elevation with its intersection

with the emitting surface (Fig. 19). Then from an elementary pixel in azimuth and elevation we must find the vertex of the quadrilateral corresponding to the elementary pixel projected on the surface of ensonification. Finally, we must calculate the area of this quadrilateral.

Case 1: The sources are located on a known sentinel surface

We suppose a vertical surface S located at a distance d from the origin, perpendicular to the y-axis (Fig. 20). A source "I" on surface S emits an incoming sound with an azimuth α and an elevation θ, then the directing vector of the line of sight connecting the origin with "I" is given by:

$$u = [u_x, u_y, u_z] = [cos(\theta)cos(\alpha), cos(\theta)sin(\alpha), sin(\alpha)] \qquad (19)$$

R the distance between the origin and the point "I" is obtained by:

$$R = \frac{d}{u_y} \qquad (20)$$

The coordinates of "I" are then:

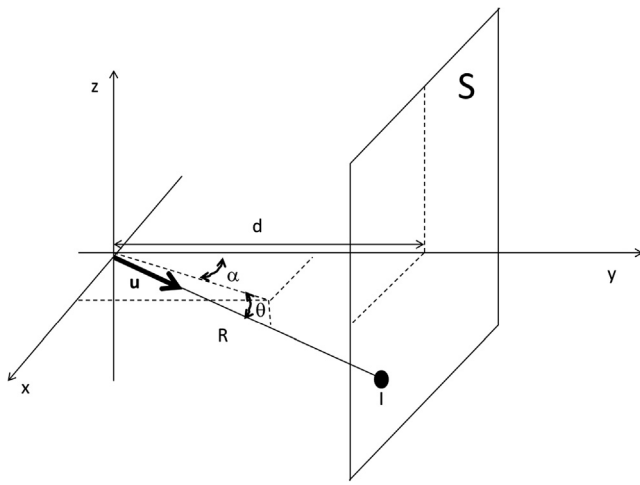$$[I_x, I_y, I_z] = \left[d\frac{u_x}{u_y}, d, d\frac{u_z}{u_y} \right] \qquad (21)$$

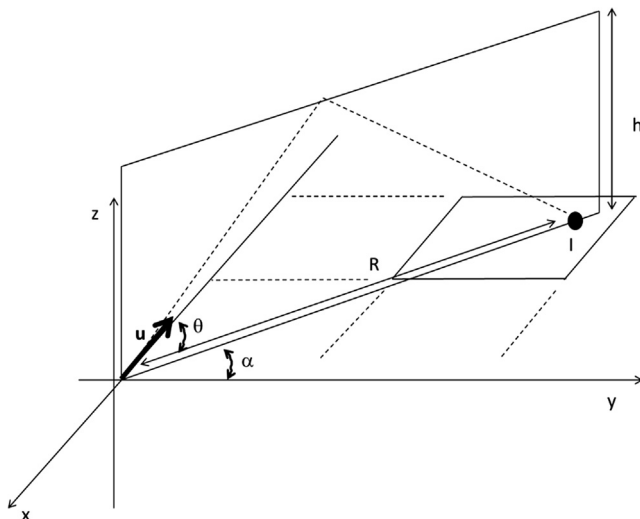**Fig. 19.** Calculation geometry for a sentinel surface representation.

Fig. 20. Calculation geometry for a source on the seabed using the reflected surface echoes for the assessment of the seafloor map.

For an elementary pixel in azimuth and elevation P : $[\alpha_0 + d\alpha/2, \alpha_0 + d\alpha/2] \times [\theta_0 - d\theta/2, \theta_0 + d\theta/2]$, the coordinates of five points are calculated: the center of the quadrilateral C (see plot P_3, Fig. 9) corresponding to $\{\alpha_0, \theta_0\}$ and the four vertex of the quadrilateral s_1 corresponding to $\{\alpha_0 - \alpha/2, \theta_0 - d\theta/2\}$, s_2 corresponding to $\{\alpha_0 - \alpha/2, \theta_0 + d\theta/2\}$, s_3 corresponding to $\{\alpha_0 + \alpha/2, \theta_0 + d\theta/2\}$, and s_4 corresponding to $\{\alpha_0 + \alpha/2, \theta_0 - d\theta/2\}$ (plot P_3, Fig. 9).

Finally, the area A of the quadrilateral is computed thanks to the coordinates of the vertex by:

$$2A = |(x_1 - x_3) \times (z_2 - z_4)| + |(x_2 - x_4) \times (z_1 - z_3)| \qquad (22)$$

where $x_1, x_2, x_3, x_4, z_1, z_2, z_3, z_4$ are the coordinates of the s_1, s_2, s_3, s_4 in the vertical surface S.

Case 2: The sources located on the seafloor using echoes reflected on the surface

We assume a source "I" located on the seabed and emitting an echo reflected on the surface and then joining the array of measurement (Fig. 20). The distance between the source "I" and the origin is referred to as "R" and the height of the water column is referred to as "h", the azimuth and the elevation of the arrival of the path reflected at the surface are α and θ. The distance "R" is given by:

$$R = 2\frac{h}{tan(\theta)} \qquad (23)$$

And the coordinates of "I" are:

$$[I_x, I_y, I_z] = [Rcos(\alpha), Rsin(\alpha), 0] \qquad (24)$$

As in the other case, for an elementary pixel in azimuth and elevation P : $[\alpha_0 + d\alpha/2, \alpha_0 + d\alpha/2] \times [\theta_0 - d\theta/2, \theta_0 + d\theta/2]$, the coordinates of five points are calculated: C (plot P_4, Fig. 9) corresponding to $\{\alpha_0, \theta_0\}$ and the four vertex of the quadrilateral s_1 corresponding to $\{\alpha_0 - \alpha/2, \theta_0 - d\theta/2\}$, s_2 corresponding to $\{\alpha_0 - \alpha/2, \theta_0 + d\theta/2\}$, s_3 corresponding to $\{\alpha_0 + \alpha/2, \theta_0 + d\theta/2\}$, and s_4 corresponding to $\{\alpha_0 + \alpha/2, \theta_0 - d\theta/2\}$ (see plot P_4, Fig. 9).

Finally the area A of the quadrilateral is computed thanks to the coordinates of the vertex by:

$$A = |(x_1 - x_3) \times (y_2 - y_4)| \times |(x_2 - x_4) \times (y_1 - y_3)| \qquad (25)$$

where $x_1, x_2, x_3, x_4, y_1, y_2, y_3, y_4$ are the coordinates of the s_1, s_2, s_3, s_4 at the seafloor.

References

[1] Krause B. Bioacoustics: habitat ambience & ecological balance. Whole Earth Rev 1987;57:14–6.

[2] Kinda GB, Simard Y, Gervaise C, Mars JI, Fortier L. Arctic underwater noise transients from sea ice deformation: characteristics, annual time series, and forcing in Beaufort Sea. J Acoust Soc Am 2015;138:2034–45. https://doi.org/10.1121/1.4929491.

[3] Mathias D, Gervaise C, Di Iorio L. Wind dependence of ambient noise in a biologically rich coastal area. J Acoust Soc Am 2016;139:839–50. https://doi.org/10.1121/1.4941917.

[4] Nystuen JA. Rainfall measurements using underwater ambient noise. J Acoust Soc Am 1986;79:972–82. https://doi.org/10.1121/1.393695.

[5] Hildebrand JA. Anthropogenic and natural sources of ambient noise in the ocean. Mar Ecol Prog Ser 2009;395:5–20.

[6] Gervaise C, Simard Y, Roy N, Kinda B, Ménard N. Shipping noise in whale habitat: characteristics, sources, budget, and impact on belugas in Saguenay–St. Lawrence Marine Park hub. J Acoust Soc Am 2012;132:76–89. https://doi.org/10.1121/1.4728190.

[7] Au WW, Hastings MC. Principles of marine bioacoustics. New York: Springer; 2008.

[8] Amorim MCP. Diversity of sound production in fish. Commun Fish 2006;1:71–104.

[9] Parmentier E, Di Iorio L, Picciulin M, Malavasi S, Lagardère J-P, Bertucci F. Consistency of spatiotemporal sound features supports the use of passive acoustics for long-term monitoring. Anim Conserv n.d. doi:10.1111/acv.12362.

[10] Di Iorio L, Raick X, Parmentier E, Boissery P, Valentini-Poirier cathy anna, Gervaise C. Posidonia meadows calling: a ubiquitous fish sound with monitoring potential. Submitt Remote Sens Ecol n.d.

[11] Ferguson BG, Cleary JL. In situ source level and source position estimates of biological transient signals produced by snapping shrimp in an underwater environment. J Acoust Soc Am 2001;109:3031–7.

[12] Johnson MW, Everest FA, Young RW. The role of snapping shrimp (Crangon and Synalpheus) in the production of underwater noise in the sea. Biol Bull 1947;93:122–38. https://doi.org/10.2307/1538284.

[13] Chitre M, Legg M, Koay T-B. Snapping shrimp dominated natural soundscape in Singapore waters. Contrib Mar Sci 2012;2012:127–34.

[14] Radford CA, Jeffs A, Tindle CT, Montgomery JC. Resonating sea urchin skeletons create coastal choruses. Mar Ecol Prog Ser 2008;362:37–43.

[15] Popper AN, Salmon M, Horch KW. Acoustic detection and communication by decapod crustaceans. J Comp Physiol A 2001;187:83–9. doi:10.1007s003590100184.

[16] Di Iorio L, Gervaise C, Jaud V, Robson AA, Chauvaud L. Hydrophone detects cracking sounds: non-intrusive monitoring of bivalve movement. J Exp Mar Biol Ecol 2012;432–433:9–16.

[17] Coquereau L, Grall J, Chauvaud L, Gervaise C, Clavier J, Jolivet A, et al. Sound production and associated behaviours of benthic invertebrates from a coastal habitat in the north-east Atlantic. Mar Biol 2016;163:1–13. https://doi.org/10.1007/s00227-016-2902-2.

[18] Sousa-Lima RS, Fernandes DP, Norris TF, Oswald JN. A review and inventory of fixed autonomous recorders for passive acoustic monitoring of marine mammals: 2013 state-of-the-industry. In: Acoust underw geosci symp RIO acoust 2013 IEEEOES; 2013. p. 1–9. doi:10.1109/RIOAcoustics.2013.6683984.

[19] Pijanowski BC, Villanueva-Rivera LJ, Dumyahn SL, Farina A, Krause BL, Napoletano BM, et al. Soundscape ecology: the science of sound in the landscape. Bioscience 2011;61:203–16.

[20] Sueur J, Farina A. Ecoacoustics: the ecological investigation and interpretation of environmental sound. Biosemiotics 2015;8:493–502. https://doi.org/10.1007/s12304-015-9248-x.

[21] Hastings PA, Širović A. Soundscapes offer unique opportunities for studies of fish communities. Proc Natl Acad Sci 2015;112:5866–7. https://doi.org/10.1073/pnas.1505897112.

[22] Merchant ND, Fristrup KM, Johnson MP, Tyack PL, Witt MJ, Blondel P, et al. Measuring acoustic habitats. Meth Ecol Evol 2015;6:257–65. https://doi.org/10.1111/2041-210X.12330.

[23] Archambault P, Bourget E. Scales of coastal heterogeneity and benthic intertidal species richness, diversity and abundance. Mar Ecol Prog Ser Oldendorf 1996;136:111–21.

[24] Garcia-Charton JA, Pérez-Ruzafa A, Sanchez-Jerez P, Bayle-Sempere JT, Renones O, Moreno D. Multi-scale spatial heterogeneity, habitat structure, and the effect of marine reserves on Western Mediterranean rocky reef fish assemblages. Mar Biol 2004;144:161–82. https://doi.org/10.1007/s00227-003-1170-0.

[25] Terlizzi A, Anderson MJ, Fraschetti S, Benedetti-Cecchi L. Scales of spatial variation in Mediterranean subtidal sessile assemblages at different depths. Mar Ecol Prog Ser 2007;332:25–39.

[26] Anderson MJ, Millar RB. Spatial variation and effects of habitat on temperate reef fish assemblages in northeastern New Zealand. J Exp Mar Biol Ecol 2004;305:191–221. https://doi.org/10.1016/j.jembe.2003.12.011.

[27] Bell JD, Westoby M. Variation in seagrass height and density over a wide spatial scale: effects on common fish and decapods. J Exp Mar Biol Ecol 1986;104:275–95. https://doi.org/10.1016/0022-0981(86)90110-3.

[28] Miller RG, Hutchison JA, Macleod AK, Burrows MT, Cook EJ, Last KS, et al. Marine renewable energy development: assessing the Benthic Footprint at multiple scales. Front Ecol Environ 2013;11:433–40. https://doi.org/10.1890/120089.

[29] Polovina JJ. Fisheries applications and biological impacts of artificial habitats. Artif Habitats Mar Freshw Fish Acad Press San Diego Calif 1991:153–76.

[30] Sathe MP, Thanner SE, Blair SM. Bal harbour mitigation artificial reef monitoring program - year 10. State of Florida: Department of Environmental Resources Management; 2010.

[31] Grossman GD, Jones GP, Seaman WJ. Do artificial reefs increase regional fish production? A review of existing data. Fisheries 1997;22:17–23. https://doi.org/10.1577/1548-8446(1997) 022<0017:DARIRF>2.0.CO;2.

[32] Bohnsack JA, Sutherland DL. Artificial reef research: a review with recommendations for future priorities. Bull Mar Sci 1985;37:11–39.

[33] Davis N, VanBlaricom GR, Dayton PK. Man-made structures on marine sediments: effects on adjacent benthic communities. Mar Biol 1982;70:295–303. https://doi.org/10.1007/BF00396848.

[34] Ambrose RF, Anderson TW. Influence of an artificial reef on the surrounding infaunal community. Mar Biol 1990;107:41–52. https://doi.org/10.1007/BF01313240.

[35] Langlois TJ, Anderson MJ, Babcock RC. Reef-associated predators influence adjacent soft-sediment communities. Ecology 2005;86:1508–19.

[36] Azevedo FBB, Carloni GG, Carvalheira LV. Colonization of benthic organisms on different artificial substratum in Ilha Grande bay, Rio de Janeiro Brazil. Braz Arch Biol Technol 2006;49:263–75.

[37] Folpp H, Lowry M, Gregson M, Suthers IM. Fish assemblages on estuarine artificial reefs: natural rocky-reef mimics or discrete assemblages? PLoS ONE 2013;8:. https://doi.org/10.1371/journal.pone.0063505e63505.

[38] Ponti M, Fava F, Perlini RA, Giovanardi O, Abbiati M. Benthic assemblages on artificial reefs in the northwestern Adriatic Sea: does structure type and age matter? Mar Environ Res 2015;104:10–9. https://doi.org/10.1016/j.marenvres.2014.12.004.

[39] Urick RJ. Principles of underwater sound for engineers. Tata: McGraw-Hill Education; 1967.

[40] Radford CA, Tindle CT, Montgomery JC, Jeffs AG. Modelling a reef as an extended sound source increases the predicted range at which reef noise may be heard by fish larvae. Mar Ecol Prog Ser 2011;438:167–74. https://doi.org/10.3354/meps09312.

[41] Piercy JJB, Smith DJ, Codling EA, Hill AJ, Simpson SD. The good, the bad, and the distant: soundscape cues for larval fish. In: Popper AN, Hawkins A, editors. Eff Noise Aquat Life II, vol. 875. New York, NY: Springer; 2016. p. 829–37.

[42] Lillis A, Eggleston DB, Bohnenstiehl DR. FEATURE ARTICLE estuarine soundscapes: distinct acoustic characteristics of oyster reefs compared to soft-bottom habitats. Mar Ecol Prog Ser 2014;505:1–17. https://doi.org/10.3354/meps10805.

[43] Freeman SE, Buckingham MJ, Freeman LA, Lammers MO, Gerald LD. Cross-correlation, triangulation, and curved-wavefront focusing of coral reef sound using a bi-linear hydrophone array. J Acoust Soc Am 2015;137:30–41.

[44] Freeman SE, Freeman LA, Lammers MO, Buckingham MJ. Spatial variation of the underwater soundscape over coral reefs in the Northwestern Hawaiian Islands. J Acoust Soc Am 2014;136:2276.

[45] Epifanio CL, Potter JR, Deane GB, Readhead ML, Buckingham MJ. Imaging in the ocean with ambient noise: the ORB experiments. J Acoust Soc Am 1999;106:3211–25. https://doi.org/10.1121/1.428175.

[46] Kuselan S, Chitre M, Pallayil V. Ambient noise imaging through joint source localization. Ocean. MTSIEEE KONA: IEEE; 2011. p. 1–5.

[47] Chitre M, Kuselan S, Pallayil V. Ambient noise imaging in warm shallow waters; robust statistical algorithms and range estimation. J Acoust Soc Am 2012;132:838–47. https://doi.org/10.1121/1.4733553.

[48] Miklovic DW, Bird MT. Snapping shrimp: measuring their natural distribution in space and time with low frequency arrays. In: MTSIEEE conf exhib OCEANS 2001, vol. 4; 2001. p. 2095–9. doi:10.1109/OCEANS.2001.968321.

[49] D'Spain GL, Batchelor HH. Observations of biological choruses in the Southern California Bight: a chorus at midfrequencies. J Acoust Soc Am 2006;120:1942–55. https://doi.org/10.1121/1.2338802.

[50] Charbonnel E, Carnus F, Ruitton S, Direac'h LL, Harmelin J-G, Beurois J. Artificial reefs in marseille: from complex natural habitats to concepts of efficient artificial reef design. In: Glob change mank-mar environ interact. Dordrecht: Springer; 2010. p. 81–2. https://doi.org/10.1007/978-90-481-8630-3_14.

[51] Radford C, Stanley J, Tindle C, Montgomery J, Jeffs A. Localised coastal habitats have distinct underwater sound signatures. Mar Ecol Prog Ser 2010;401:21–9.

[52] Lillis A, Eggleston DB, Bohnenstiehl DR. Soundscape variation from a larval perspective: the case for habitat-associated sound as a settlement cue for weakly swimming estuarine larvae. Mar Ecol Prog Ser 2014;509:57–70. https://doi.org/10.3354/meps10917.

[53] Blondel P. Continental margins. Handb. Sidescan Sonar, Berlin, Heidelberg: Springer; 2009. p. 147–83. doi:10.1007/978-3-540-49886-5_7.

[54] Patek SN. Spiny lobsters stick and slip to make sound. Nature 2001;411:153–4.

[55] Kinda GB, Simard Y, Gervaise C, Mars JI, Fortier L. Under-ice ambient noise in Eastern Beaufort Sea, Canadian Arctic, and its relation to environmental forcing. J Acoust Soc Am 2013;134:77–87.

[56] Kay SM. Fundamentals of statistical signal processing. In: Oppenheim AV, editor. Vol. II: detection theory, Prentice Hall signal processing series. Prentice Hall PTR; 1998.

[57] Kay SM. Fundamentals of statistical signal processing. In: Oppenheim AV, editor. Vol. I: estimation theory, Prentice Hall signal processing series. Prentice Hall PTR; 1993.

[58] Aubauer R, Lammers MO, Au WWL. One-hydrophone method of estimating distance and depth of phonating dolphins in shallow water. J Acoust Soc Am 2000;107:2744–9. https://doi.org/10.1121/1.428660.

[59] Lossent J, Di Iorio L, Valentini-Poirier C, Boissery P, Gervaise C. Mapping the diversity of spectral shapes discriminates between adjacent benthic biophonies. Mar Ecol Prog Ser 2017;585:31–48. https://doi.org/10.3354/meps12370.

[60] Erbe C, Williams R, Sandilands D, Ashe E. Identifying modeled ship noise hotspots for marine mammals of Canada's Pacific Region. PLoS ONE 2014;9:. https://doi.org/10.1371/journal.pone.0089820e89820.

[61] Cato DH, Bell MJ. Ultrasonic ambient noise in Australian shallow waters at frequencies up to 200 kHZ; 1992.

[62] McWilliam JN, Hawkins AD. A comparison of inshore marine soundscapes. J Exp Mar Biol Ecol 2013;446:166–76.

[63] Cato DH. The biological contribution to the ambient noise in waters near Australia. Aoucstics Aust - Spec Issue Underw Acoust 1992;20:76–80.

[64] de Marseille Ville. Synthèse opération RECIFS PRADO. Ville de Marseille Publ.; 2014.